HANDBOOK OF NUCLEAR WEAPON EFFECTS

Calculational Tools Abstracted From DSWA's Effects Manual One (EM-1)

John Northrop

HANDBOOK OF
NUCLEAR WEAPON EFFECTS

Calculational Tools Abstracted From EM-1

1st Edition
September 1996

DECLASSIFIED; UNCLASSIFIED; NOT SECRET!!

PREFACE

At the time of publication of the Defense Special Weapons Agency's (DSWA) eighth edition of *Effects Manual One*(EM-1)*, which was completed in 1993, it was recognized that its easy use would be limited by both its length and its classification. This work, *EM-1 Technical Handbook*, addresses those limitations. It is designed for the engineer who has a working knowledge of nuclear weapon effects and, thus, does not need the extensive tutorial sections of the basic *EM-1*. It includes algorithms, graphs, and tables required to make approximate quantitative estimates of nuclear weapon effects, along with a brief description of their use.

Of the twenty-two volumes of *EM-1*, five were judged inappropriate for this handbook, either as a result of their extensive classified database or because they were almost entirely qualitative and tutorial. In addition, Volume 1, containing synopses of the other volumes, has been omitted. The chapter numbering in this handbook maintains the nomenclature of the main *EM-1*, with consequent gaps for the omitted volumes. Most of the Sample Problems from *EM-1*, judged helpful in understanding the application of the algorithms, have been included but in a more compressed form. Other sacrifices, primarily in type font and figure size, have been made to allow the handbook to be printed in a single volume. Additionally, to save space, all the primary source references in *EM-1*, both for specific data used as well as extensive bibliographies, have been deleted in this handbook. Readers requiring more detailed information are referred to the original *EM-1*, for which all except Volumes 1, 3, and 13 are classified.

The actual publication date of each *EM-1* volume is indicated below. Because of the lengthy writing, review, and publication process, the actual age of the technology provided is approximately five years before this date. For the current status of the contents of any *EM-1* chapter, write to the Weapons Effects Division, Defense Special Weapons Agency, 6801 Telegraph Road, Alexandria, VA 22310-3398. Since the Editor of this handbook has simply abstracted the material from the basic multi-volume series, with some liberties taken in compressing text, the following authors of the source volumes of *EM-1* deserve full credit:

Vol. 2: D.C. Sachs, E. Martin (Kaman Sciences); L. Kennedy, G. Schneyer, J. Barthel, T. Pierce, C. Needham (Maxwell Laboratories); and J. Keefer, N. Ethridge; (1985).

Vol. 3: C.K.B. Lee, L.P. Mosteller, and T.A. Mazzola (Logicon RDA); E.J. Rinehart, (DSWA), A.V. Cooper, and S.H. Schuster (California Research and Technology Corp.); (1992).

Vol. 4: J.E. Cockayne and D.P. Bacon (SAIC); T.A. Mazzola (Logicon RDA); M. Rosenblatt (The Titan Corporation), and J.A. Northrop, Editor (S-Cubed); (1992).

Vol. 5: R.M. Barash, J.A. Goertner, and G.A. Young (Naval Surface Warfare Center); C.B.K. Lee (Logicon RDA); B.B. LeMehaute (University of Miami); and J.P. Moulton (Kaman Sciences); (1991).

Vol. 6: J.R. Keith and D.C. Sachs (Kaman Sciences); (1985).

Vol. 7: D. Steel, J.R. Keith, H.D. Bos, and E.J. Plute, Jr., (Kaman Sciences); H.C. Lindberg (APTEK, Inc.); (1987, 1993).

Vol. 8: D.C. Kaul, F.Dolatshahi, W.A. Woolson, and W.Scott (SAIC); H.G. Norment (ASI); (1990).

Vol. 9: W. Knapp and B. Gambill (Kaman Sciences); (1986).

Vol. 10: E. Quinn (Technical Integrator), J. Schlegel and W. Kehrer (Logicon RDA), C. Fore (Editor) and T. Stringer (Kaman Sciences), R. Schaefer and W. Radasky (Metatech), G. Morgan (TRW), and K. Casey and B. Stewart (JAYCOR); (1992).

TABLE OF CONTENTS

Figure 7.8. ANISN Deposition Profile for Aluminum at Blackbody Temperatures of 1, 5, and 10 keV (Incident Fluence = 1 cal/cm^2).
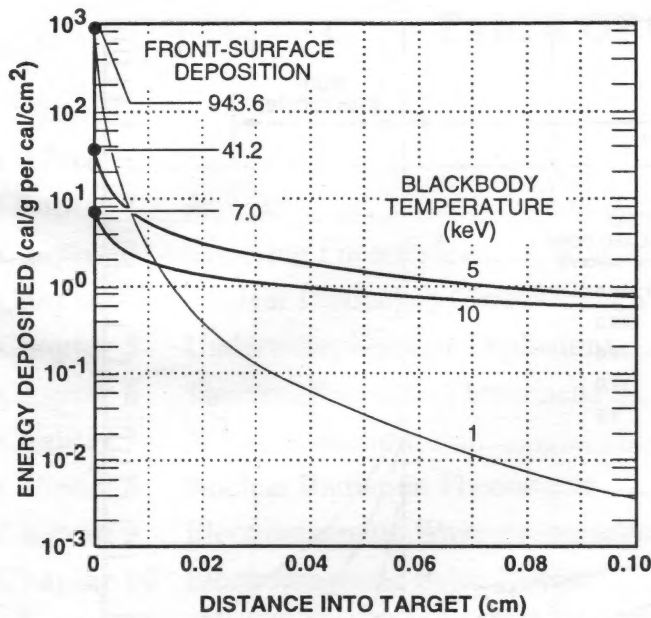

Figure 7.9. ANISN Deposition Profile for Iron at Blackbody Temperatures of 1, 5, and 10 keV (Incident Fluence = 1 cal/cm^2).

Material response occurs on a time scale comparable to the wall thickness, while structural response occurs on a time scale comparable to structural dimensions such as body diameter. Nosetips and antenna windows have lateral dimensions comparable to thickness, so must be treated by three-dimensional shock codes that do not distinguish between shock and structural response.

7.2.2.1 Stress Wave Generation and Propagation. The dominant modes of material shock response are often those of shock generation and reverberation through the thickness of a structural wall, with negligible lateral effect. The following discussion develops simple one-dimensional equations of motion and wave theory.

Cold x rays (blackbody photon energies less than about 2 keV) have small absorption depths, de-

Figure 7.10. ANISN Deposition Profile for Tantalum at Blackbody Temperatures of 1, 5, and 10 keV (Incident Fluence = 1 cal/cm^2).

positing most of their energy near the front surface of a material. Hot x rays (blackbody energies greater than about 10 keV) have much greater absorption depths, and significant absorption occurs throughout the thickness of a material. Representative deposition profiles in a two-layered wall, consisting of an organic composite heatshield and a metal base structure, are shown in Figure 7.11. These doses are normalized to an incident fluence of 1 cal/cm^2. The materials and thicknesses are typical of those used for a reentry vehicle aeroshell.

Immediately after energy deposition, the pressure P(t) in the material is given by

$$P(t) = \Gamma \rho_o E_D(x), \tag{7.45}$$

where Γ is the Grüneisen ratio and is a property of the material, ρ_o is the initial material density, and $E_D(x)$ is the deposited energy at depth x into the material. Γ may be estimated from thermal expansion data using the following relation:
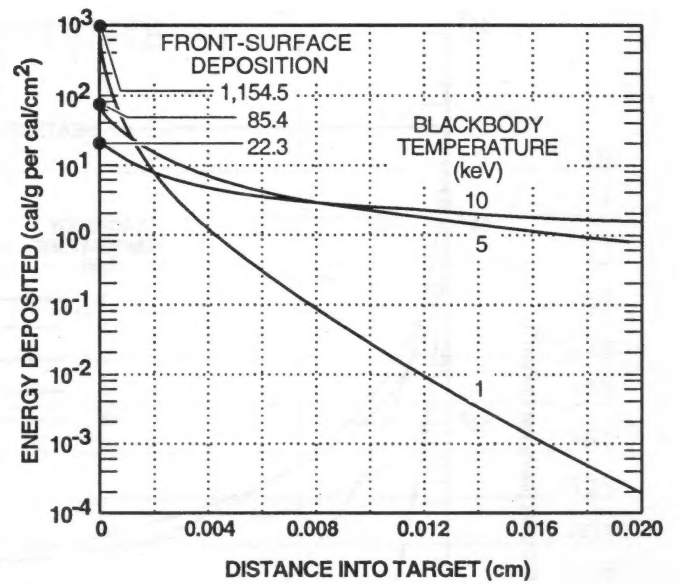
$$\Gamma = C\alpha / \left(\rho_o c_p \right) \tag{7.46}$$

279

Figure 7.11. X-Ray Energy Deposition in a Typical Heatsheld and Substructure for Blackbody Temperatures From Cold to Hot (1 to 10 keV) (Doses Normalized to an Incident Fluence of 1 cal/cm²).

where C is the bulk modulus at low pressures, α is the *volumetric* coefficient of thermal expansion, and c_P is the specific heat at constant pressure. The value for Γ from Equation 7.46 should be relied upon only if all material property values are for the same density, pressure, and temperature. For many materials, the value of Γ lies between 1.0 and 2.0, with metals tending to have the higher values.

7.2.2.1.1 Deposition-Time Stress Relief.

These discussions have all treated energy deposition as near-instantaneous, although it actually occurs over a finite time, which can result in lower peak stresses. The significance of the deposition timing depends on whether $2c\tau \ll \delta$ or $2c\tau \gg \delta$, where c is the wave speed, τ is the full width at half maximum (FWHM) of the deposition time, and δ is the effective depth of energy deposition from the free surface. For an exponential deposition, δ is the e-folding depth (i.e., the depth at which the energy deposition is $1/e = 0.37$ of the value at the material surface), whereas for a triangular deposition (linear drop from the surface) δ is two-thirds the ultimate depth of deposition. The resulting peak axial stresses σ_x for linear, elastic response are given by

$$\sigma_x(\text{max}) = \Gamma\rho\frac{D_o\delta}{2c\tau}\left[1 - \exp\{-2c\tau/\delta\}\right] \text{ for compressive response, and} \tag{7.47}$$

$$\sigma_x(\text{min}) = -\Gamma\rho\frac{D_o\delta}{2c\tau}\left[1 - \exp\{-c\tau/\delta\}\right] \times \left[1 - \exp\{-2x/\delta\}\right] \tag{7.48}$$

for tensile response, where Γ is the Grüneisen ratio [Equation 7.46], ρ is the density, D_o is the peak surface energy deposition, and x is the depth into the material from the incident surface.

When $2c\tau \ll \delta$, the result is σ_x (max) $\rightarrow \Gamma\rho D_o$, which is the previously discussed condition of "instantaneous" deposition. However, if $2c\tau \gg \delta$,

$$\sigma_x(max) \rightarrow \Gamma\rho D_o\delta / (2c\tau) \tag{7.49}$$

so the peak stress drops inversely with deposition time. The peak compressive stress occurs at $t = \tau$ (end of deposition) and at the depth $x = c\tau$, whereas the peak tension occurs after deposition and asymptotically reaches a maximum with increasing depth from the free surface.

The stress history at a small depth x from the surface, with $x \ll \delta$, is given by

$$\sigma_x(max) = -\sigma_x(min) = \Gamma\rho \frac{D_o x}{c\tau} \quad . \tag{7.50}$$

7.2.2.1.2 Stress Wave Attenuation. The basic mechanism of stress wave attenuation is the reduction of the compressive stress at the peak of a shock wave by rarefactions (tensile stress waves) from a free or low-impedance surface. That is, as a stress wave propagates into a material, rarefactions from this surface continually overtake the stress peak and decrease its magnitude. This is accompanied by an increase in pulse duration and, hence, wavelength to conserve momentum within the wave. Wave energy is given up to heat in the process; kinetic energy varies as the square of the particle velocity and pressure. As the pressure drops, the wave energy per unit distance decreases faster than the increase in wavelength. This energy loss can also be viewed as conventional hysteresis in a pressure-volume plot of the loading and unloading paths. A loading-unloading path in a porous material results in a large hysteresis loop. The resulting energy loss gives very rapid stress attenuation in porous materials.

Figure 7.12 is an example of shock attenuation versus distance in a representative heatshield material, tape-wound silica phenolic. The attenuation shown is caused by its porosity as well as the increase in wave velocity with pressure. Attenuation is very rapid at higher pressures and fairly small at pressures of about 10 kbars and lower. At still higher pressures of about 200 kbars produced by cold x rays, the rate of attenuation is even more rapid.

7.2.2.1.3 Shock Wave Reflection From a Free Surface. Damage is generally the result of shock wave reflection from free or low-impedance surfaces. Damage can be caused by the high compressive stresses as they propagate through the target wall, but this damage is generally secondary compared with damage from later tensile stresses produced by reflection from a free surface. By the time a stress wave from cold or warm x rays reaches the rear free surface of a target wall, it generally has a triangular-shaped wave front because of the shock attenuation mechanisms just discussed.

Transmission and reflection of an elastic triangular wave from a free surface is illustrated in Figure 7.13. This process is conveniently visualized as the superposition of two waves: (1) a transmitted wave that continues as a ghost wave (short dashes) beyond the free surface, and (2) a reflected wave with an incoming ghost component beyond the free surface. The reflected wave is tensile and has a phase complementary to the transmitted wave relative to the free surface such that its magnitude at the free surface is equal and opposite to the incoming wave, in order to meet the stress-free boundary condition. In Figure 7.13(a), both waves are drawn as positive so that this equality of stress and complementary phase are apparent.
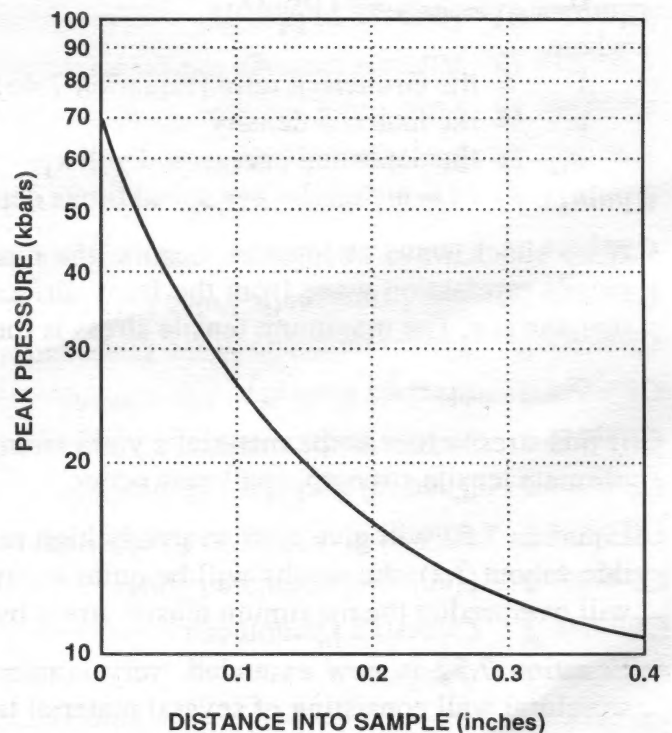
Figure 7.12. Shock Attenuation in Tape-Wound Silica Phenolic for a 10-ktap Pulse.

The total stress in the material is the sum of the incident and reflected waves, or the incident wave minus the reflected wave in the construction. Thus, proceeding from left to right in the total stress plot, the stress is equal to the incident stress until the reflected shock arrives. Then the stress drops by the magnitude of the shock jump, resulting in tension. The magnitude of the tension is the excess of the reflected tension above the incident compression. Until the reflected jump reaches the tail of the incoming wave, the slope of the stress-distance plot of total tension is twice that of the incident shock wave. Thus, tensile damage from the stress waves tends to be more concentrated near the rear surface than might first be imagined from the length of the incoming compressive wave. If no damage occurs as the reflected wave continues beyond the tail of the incoming wave, the total stress assumes the shallower slope of the incoming wave, as seen in the last of the three sketches in Figure 7.13(b).
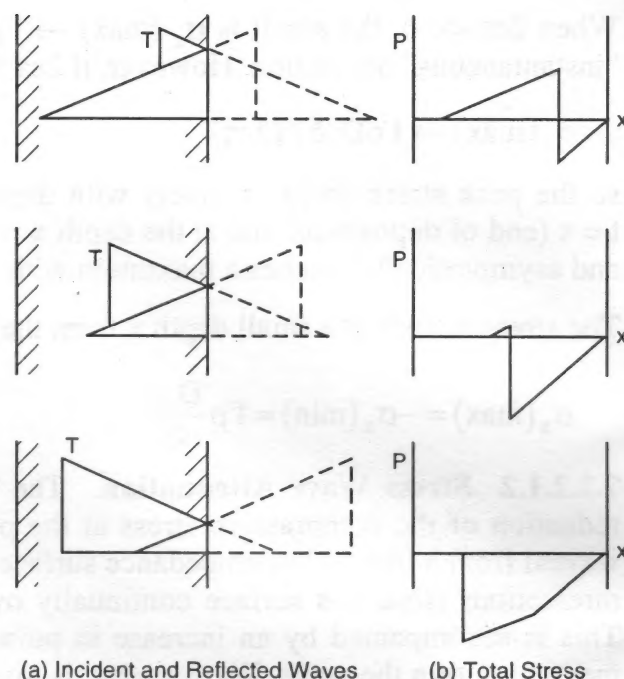

(a) Incident and Reflected Waves   (b) Total Stress

Figure 7.13. Shock Transmission and Reflection at a Free Interface.

7.2.2.2 Stress Wave Calculational Methods.

7.2.2.2.1 Simple Analytical Methods.
The application of simple analytical methods to stress wave response is extremely limited. The nature of the problem, when considering shock attenuation and the interaction between the trailing tensile rarefaction wave and the reflected rarefaction wave from the rear surface, nearly always requires a hydrocode analysis. If a structure wall consists of several layers of materials, such as a heatshield, bond, and substrate, the problem becomes even more complex and dictates the use of a hydrocode to determine the stress wave response. Nevertheless, the manual method presented in the following paragraphs may be used to simply bound the problem for a thin wall composed of a single material.

From Equation 7.45, the maximum compressive stress σ_x in the material is

$$\sigma_{x(\text{max compressive})} = \Gamma \rho E_D(x_1), \tag{7.51}$$

where

Γ = the Grüneisen ratio [Equation 7.46]
ρ = the material density,
E_D = the deposited energy at depth x_1
x_1 = $c\tau$ = material wave speed times deposition time.

If no shock wave attenuation occurs, the maximum tensile stress will occur where the trailing tensile rarefaction wave from the front surface intersects the reflected rarefaction wave from the rear surface. The maximum tensile stress is then

$$\sigma_{(\text{max tension})} = 2\, \Gamma \rho E_D(x_1). \tag{7.52}$$

If this stress exceeds the material's yield strength, yielding *may* occur. If it exceeds the material's ultimate tensile strength, spall *may* occur.

Equation 7.52 will give conservatively high results for the single-material wall. If the wall is very thin (about 2ct), the results will be quite accurate. As the wall thickness increases, Equation 7.52 will overpredict the maximum tensile stress by an increasing amount.

Equation 7.52 is now extended, very conservatively, to include maximum tensile stress for a structural wall consisting of several material layers as follows:

$$\sigma_{\text{max tension}} = 2\left\{ E_D(c_1\tau)\, \rho_1\, \Gamma_1 + \sum_{i=2}^{n} \left(E_{DO}\right)_i\, \rho_i\, \Gamma_i \right\}, \tag{7.53}$$
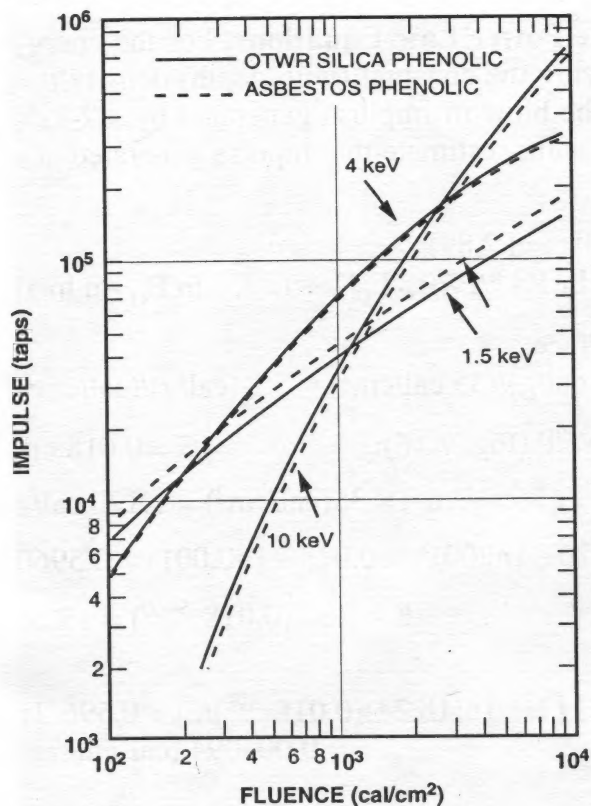
Figure 7.15. Impulse Intensity Versus Fluence in Typical Heatshield Materials for Cold, Warm, and Hot Blackbody X-Ray Spectra.

Figure 7.16. Normalized Energy Deposition Curves in TWCP for Several Blackbody Temperatures.

material (Figures 7.16 and 7.17). The energy deposition is then in the form:

$$E(z) = Kz^{-n}, \tag{7.89}$$

where the negative sign reflects the negative slope of this line; i.e., n is the absolute value of the slope, and K is an open parameter obtained by fitting Equation 7.89 to the log-log energy deposition profile.

Impulse is:　　$I = C\phi^{1/n}, \tag{7.90}$

where C is an open parameter obtained by fitting Equation 7.90 to measured or calculated impulse values. The important assumptions in Equation 7.90 are that impulse is produced by processes that do not depend on rates (for example, viscosity is unimportant) or on the microdimensions of the material (such as fiber size in composite materials). These same assumptions are also made in most of the standard hydrocodes and in the semianalytical impulse formulas.

Substituting Equation 7.89 into Equations 7.88 and 7.87 and integrating gives the following formula for impulse:

$$I = 1.6971 \, \rho \left\{ \frac{K\bar{z}^{(2-n)}}{(2-n)} - \frac{\bar{z}^2 E_o}{2} \left[1 + \ln \frac{K\bar{z}^{-n}}{E_o} + \frac{n}{2} \right] \right\}^{1/2} \tag{7.91}$$

Figure 7.17. Normalized Energy Deposition Curves in TWSP for Several Blackbody Temperatures.

8. NUCLEAR RADIATION PHENOMENA

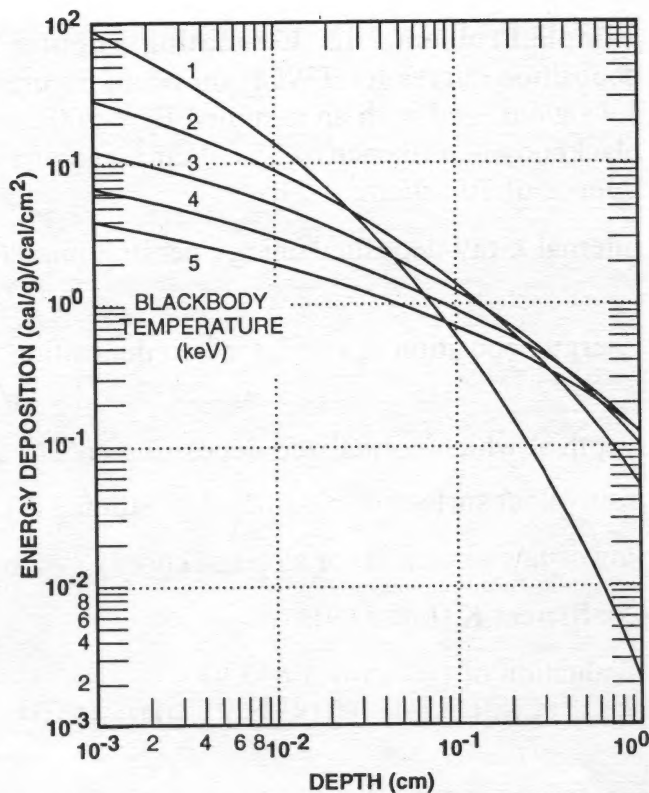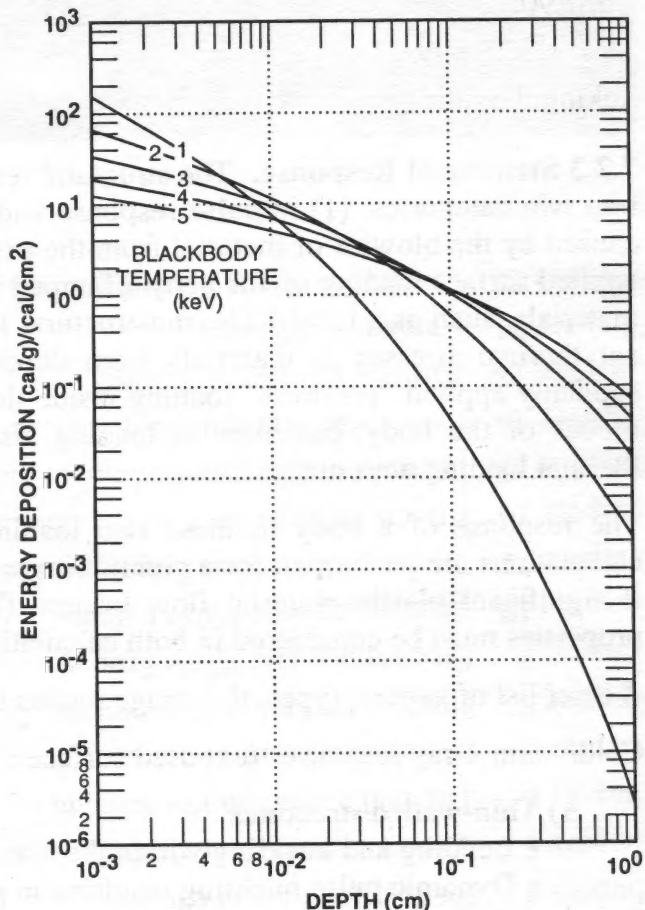**8.1 Introduction.** Although the radiation from nuclear explosions includes gamma rays, neutrons, beta particles, and alpha particles, only the first two elements are transported over significant distances through matter, and thus are the only ones considered in detail in this chapter. The exceptions to this are high-altitude explosions in which beta-particle phenomena occur over large distances, and direct contact with fallout in which beta particles, and to a lesser extent and only at very late times, alpha particles, may be significant.

Radiation from a nuclear explosion is generally considered in two categories: initial (< 1 min) and residual (> 1 min). Initial radiation is further subdivided into prompt radiation: neutrons and gamma rays produced in the weapon fission and fusion processes; secondary radiation: gamma rays produced by neutron interactions with material (air, ground, structures) outside the weapon; and delayed radiation: fission-product neutron and gamma rays, and neutron activation gamma rays. Residual radiation includes fallout from debris clouds (fission debris, weapon activation products, and entrained environmental activation products) and activation radiation from neutron capture in environmental material not entrained in the debris cloud. Table 8.1 lists these components, their approximate emission times, and their energy range. Figure 8.1 shows an idealized, normalized gamma-ray output, both with and without those arising from neutron interaction in the atmosphere.

Table 8.1. Approximate Emission Times and Energy Ranges of the Components of Radiation from Nuclear Weapons.

RADIATION COMPONENT	EMISSION TIME	ENERGY RANGE (MeV)
Prompt Radiation		
- Fission neutrons	< 0.01 μ sec	0 - 10
- Fusion neutrons	< 0.01 μ sec	14
- Fission gamma rays	< 0.01 μ sec	0.012 - 6
Secondary Gamma Rays		
Inelastic-scattering gamma rays from:		
- Weapon	< 0.01 μ sec	—
- Nitrogen	< 10 μ sec	0.7 - 7
- Oxygen	< 10 μ sec	2 - 7
- Elements in ground/structures	< 10 μ sec	0 - 8
Capture gamma rays from:		
- Weapon	< 0.01 μ sec	—
- Nitrogen	Few ms - 0.03 sec	1.5 - 11
- Oxygen (negligible)	—	
- Elements in ground/structures	Few ms - 0.03 sec	0 - > 9
Delayed Radiation		
- Fission-product neutrons	< 1 minute	0 - 5
- Fission-product gamma rays	1 ms - 1 minute	0 - 8
- Activation gamma rays	1 ms - 1 minute	0 - 2
Residual Radiation		
Fallout radiation:		
- Fission-product gamma rays	1 min. - many years	0 - 8
- Weapon activation gammas	1 min. - many years	—
- Environmental activation gammas	Tens of years	0 - 2
- Non-entrained environmental gammas	Tens of years	0 - 2

8.2 Initial Nuclear Radiation.

8.2.1 Definitions and Numerical Values.

Flux ($\dot{\phi}$): The particle track length per unit volume per unit time, or equivalently, the product of the particle density, i.e., number per cubic centimeter, and the particle speed ($\dot{\phi} = nv$). The flux is expressed as particles per square centimeter per second.

Fluence (ϕ): The particle track length per unit volume, or equivalently, the product (or integral) of particle flux and time ($\phi = nvt$), expressed as particles per square centimeter.

Dose (D): The amount of energy absorbed from the radiation per gram of absorbing material. The traditional unit of dose is the rad (= 100 ergs/g). The International System of Units dose quantity is the gray (= 100 rads). A centigray equals 1 rad. Since the ability of radiation to deposit energy in a given material is governed by the reaction cross sections of that material for the particular radiation involved, the material in which the dose is deposited must be stipulated: thus, rads (tissue) or rad (Si).
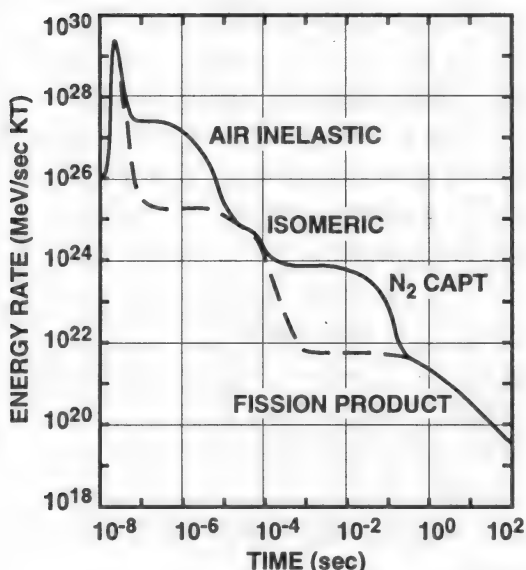

Figure 8.1. Idealized Time Dependence of the Gamma-Ray Output from a Large Yield Explosion, Normalized to 1 KT.

Dose rate ($\dot{D}$): The rate (per unit time) at which absorbed dose is accumulated.

Kerma (kinetic energy released in material): The amount of energy imparted to charged particles by neutral particles per unit mass of target material. Units of kerma are the same as those of dose. It differs from rads in that the energy is only imparted to charged particles in reactions within the unit mass, but this charged particle energy is not necessarily deposited within the unit mass, which is the criterion for rads. In practice, the energy deposited by charged particles at a given location is almost never determined because of the difficulty of such calculations and because the range of charged particles is much less than that of neutral particles in a given medium. Therefore, a condition of charged-particle equilibrium is assumed to exist in which losses of charged particles produced at a given location are balanced by the gain of particles from adjacent sites. This assumption allows dose to be equated with kerma and they will be used rather interchangeably in this chapter. Kerma for soft tissue and for silicon are provided in Tables 8.2 and 8.3 for neutrons and gamma rays, respectively.

Kerma rate: The rate (per unit time) at which kerma is accumulated.

Free field: The intensity of initial radiation in the absence of shielding local to the detector or target.

Fusion: The nuclear reaction (combination) of two light nuclei to form a heavier nucleus. The fusion reaction having the highest probability of occurrence is that between deuterium and tritium:

$^2D_1 + {}^3T_1 = {}^4He_2 + {}^1n_0 + 17.6$ MeV. Approximately 14 MeV of this reaction energy is carried off as kinetic energy of the resulting neutron, and the remaining by the helium ion.

Table 8.2. Neutron Kerma by Energy Groups.

	UPPER GROUP BOUNDARY (MeV)	TISSUE DOSE (rad[tissue]/n/cm^2)	IONIZING SILICON DOSE (rad[Si]/n/cm^2)	1-MeV NEUTRON EQUIVALENT DAMAGE FLUENCE IN SILICON (n/cm^2)/(n/cm^2)
	14.918	6.6327×10^{-9}	1.0103×10^{-9}	2.2224
1	12.214	6.1563×10^{-9}	9.1268×10^{-10}	2.1203
2	10.000	5.6470×10^{-9}	7.1390×10^{-10}	1.9783
3	8.1873	5.2725×10^{-9}	4.0598×10^{-10}	2.0091
4	6.3763	4.7306×10^{-9}	1.4966×10^{-10}	2.0437
5	4.9659	4.4767×10^{-9}	8.5471×10^{-11}	1.7573
6	4.0657	4.2223×10^{-9}	5.8964×10^{-11}	1.4102
7	3.0119	3.5762×10^{-9}	6.6914×10^{-11}	1.8662
8	2.3852	3.2121×10^{-9}	5.0890×10^{-11}	1.5552
9	1.8268	2.7753×10^{-9}	2.5495×10^{-11}	8.8346×10^{-1}
10	1.1080	2.1072×10^{-9}	2.0337×10^{-11}	8.9212×10^{-1}
11	5.5023×10^{-1}	1.3089×10^{-9}	1.1842×10^{-11}	6.5751×10^{-1}
12	1.5764×10^{-1}	8.0649×10^{-10}	5.9340×10^{-13}	4.1182×10^{-2}
13	1.1109×10^{-1}	4.2273×10^{-10}	5.1437×10^{-13}	4.2761×10^{-2}
14	2.1875×10^{-2}	7.1195×10^{-11}	6.1825×10^{-14}	7.4376×10^{-3}
15	1.2341×10^{-3}	4.9812×10^{-12}	3.2015×10^{-15}	6.0524×10^{-4}
16	1.0130×10^{-4}	1.0808×10^{-12}	6.8608×10^{-16}	8.9113×10^{-5}
17	2.9023×10^{-5}	1.0006×10^{-12}	7.8884×10^{-16}	1.0103×10^{-4}
18	1.0677×10^{-5}	1.4760×10^{-12}	1.2572×10^{-15}	1.4131×10^{-4}
19	3.0590×10^{-6}	2.5611×10^{-12}	2.2895×10^{-15}	2.4446×10^{-4}
20	1.1254×10^{-6}	3.7144×10^{-12}	3.9798×10^{-15}	4.2203×10^{-4}
21	4.1399×10^{-7}	1.4969×10^{-11}	1.4942×10^{-14}	1.5817×10^{-3}
22	1.0000×10^{-11}			

Table 8.3. Gamma-Ray Kerma by Energy Group.

	UPPER GROUP ENERGY BOUNDARY (MeV)	TISSUE DOSE (rad[tissue] / γ /cm^2)	SILICON DOSE (rad[Si]/ γ /cm^2)
1	12.00	2.7272×10^{-9}	3.5851×10^{-9}
2	10.00	2.3471×10^{-9}	2.9440×10^{-9}
3	8.00	2.0616×10^{-9}	2.4850×10^{-9}
4	7.00	1.8496×10^{-9}	2.1750×10^{-9}
5	6.00	1.6445×10^{-9}	1.8620×10^{-9}
6	5.00	1.4352×10^{-9}	1.5450×10^{-9}
7	4.00	1.2152×10^{-9}	1.2220×10^{-9}
8	3.00	1.0412×10^{-9}	9.8030×10^{-10}
9	2.50	9.0414×10^{-10}	8.2840×10^{-10}
10	2.00	7.5648×10^{-10}	6.7180×10^{-10}
11	1.50	5.8513×10^{-10}	5.0740×10^{-10}
12	1.00	4.2645×10^{-10}	3.6810×10^{-10}
13	7.00×10^{-1}	2.9573×10^{-10}	2.6570×10^{-10}
14	4.50×10^{-1}	1.9196×10^{-10}	1.8410×10^{-10}
15	3.00×10^{-1}	1.0378×10^{-10}	1.1200×10^{-10}
16	1.50×10^{-1}	5.1977×10^{-11}	7.4540×10^{-11}
17	1.00×10^{-1}	3.2540×10^{-11}	1.1137×10^{-10}
18	4.50×10^{-2}	6.0114×10^{-11}	9.9441×10^{-10}
	1.00×10^{-2}		

Relationship between neutron energy and velocity:

$$v = 1.38 \times 10^9 \, (\text{MeV})^{1/2} \text{ in units of cm/sec.}$$

Fission: The splitting apart of a heavy nucleus into (generally) two smaller nuclei accompanied by the release of several neutrons (on average) and gamma-rays. The fissioning of U^{235}, U^{238}, and Pu^{239} following capture of a neutron are the relevant fission reactions in nuclear weapons. Each fission releases about 200 MeV of energy, primarily carried off a kinetic energy of the fission fragments, with about 180 MeV contributing to the force of the explosion. 1 KT is equivalent to approximately 1.45×10^{23} fissions.

Hydrodynamic enhancement: The increase in dose arising from the reduced area density of air through which delayed gamma rays are transmitted as a result of the explosion energy displacing a large volume of air into a shell at a larger radius than its pre-explosion distribution.

Standard atmosphere: Refer to Table 2.1 in Chapter 2, Airblast.

8.2.2 Weapon Radiation Sources.

8.2.2.1 Generic Weapon Types. *EM-1* contains a complete description of 13 generic weapon types and extensive data on the atmospheric transport of their several types of radiation outputs. Table 8.4 is an abstract of four of these types. In general, the data in this handbook are the subset of the *EM-1* data for these types.

Table 8.4. Representative Types of Nuclear Weapons.

TYPE	DESCRIPTION
3	Unboosted fission implosion weapon, contemporary design
5	Boosted fission implosion weapon, modern design
8	Thermonuclear secondary
13	Enhanced radiation thermonuclear secondary

8.2.2.2 Neutron Sources. Figure 8.2 shows notional fission, thermonuclear, and fusion weapon source spectra (not those from Table 8.4) as well as their spectra after transport through 1 km of moist air: $\rho = 1.122 \times 10^{-3}$ g/cm^3, water 0.56 percent by weight. Both the initial and transported spectra are normalized to unity. The detailed transport calculations presented by weapon type which follow have used the neutron output (neutrons per KT) and spectrum, normalized to one neutron, as shown in Table 8.5

8.2.2.3 Gamma-Ray Sources. For most weapon designs (Table 8.6), the range of gamma-ray production efficiency as a percent of total yield ranges from 0.1 to 0.5 percent, with the larger gamma yields attributed to those weapons that are physically the smallest. Average gamma-ray energy depends more on the origin of the weapon yield (fission or fusion) and the physical size of the weapon than on the yield itself. Small weapons and those that obtain a large fraction of their yield from the fusion process tend to have the highest average gamma ray energies. Source and transported spectra for prompt and fission-product gamma radiation are shown in Figure 8.3 for the same notional weapons as used in Figure 8.2. Transport is through 1 km of uniform moist air, unperturbed by blast effects, as specified in Section 8.2.2.2. Source and transported values are normalized to unit source and unit fluence, respectively. Figure 8.4 shows normalized secondary gamma-ray spectra at a distance of 1 km in the same uniform moist air for the fission, thermonuclear, and fusion neutron sources, as shown in Figure 8.2.

Table 8.5. Neutron Source Spectra and Output for Types 3, 5, 8, and 13.

ENERGY RANGE (MeV)		NEUTRONS PER MeV			
UPPER	LOWER	SOURCE 3	SOURCE 5	SOURCE 8	SOURCE 13
1.49×10^1 – 1.22×10^1		8.85×10^{-5}	9.47×10^{-3}	1.65×10^{-2}	1.42×10^{-1}
1.22×10^1 – 1.00×10^1		5.63×10^{-4}	2.38×10^{-3}	5.49×10^{-3}	2.03×10^{-2}
1.00×10^1 – 8.19×10^0		2.06×10^{-3}	3.14×10^{-3}	3.86×10^{-3}	2.11×10^{-2}
8.19×10^0 – 6.38×10^0		5.26×10^{-3}	6.27×10^{-3}	6.00×10^{-3}	2.06×10^{-2}
6.38×10^0 – 4.97×10^0		1.34×10^{-2}	1.59×10^{-2}	1.25×10^{-2}	2.33×10^{-2}
4.97×10^0 – 4.07×10^0		2.81×10^{-2}	3.05×10^{-2}	2.22×10^{-2}	2.74×10^{-2}
4.07×10^0 – 3.01×10^0		4.19×10^{-2}	4.59×10^{-2}	3.39×10^{-2}	3.05×10^{-2}
3.01×10^0 – 2.31×10^0		8.11×10^{-2}	8.76×10^{-2}	5.85×10^{-2}	4.87×10^{-2}
2.31×10^0 – 1.83×10^0		1.37×10^{-1}	1.44×10^{-1}	9.75×10^{-2}	8.65×10^{-2}
1.83×10^0 – 1.11×10^0		1.85×10^{-1}	1.89×10^{-1}	1.42×10^{-1}	9.83×10^{-2}
1.11×10^0 – 5.50×10^{-1}		2.88×10^{-1}	2.99×10^{-1}	2.73×10^{-1}	1.23×10^{-1}
5.50×10^{-1} – 1.58×10^{-1}		4.37×10^{-1}	4.56×10^{-1}	4.77×10^{-1}	2.12×10^{-1}
1.58×10^{-1} – 1.11×10^{-1}		4.56×10^{-1}	4.85×10^{-1}	6.82×10^{-1}	2.27×10^{-1}
1.11×10^{-1} – 2.19×10^{-2}		1.27×10^0	1.11×10^0	2.25×10^0	5.93×10^{-1}
2.19×10^{-2} – 1.23×10^{-3}		3.50×10^0	5.15×10^0	4.10×10^0	1.93×10^{-1}
1.23×10^{-3} – 1.01×10^{-4}		7.08×10^1	1.22×10^1	4.42×10^0	5.01×10^0
1.01×10^{-4} – 2.90×10^{-5}		2.29×10^2	2.72×10^0	4.61×10^0	0.00×10^0
2.90×10^{-5} – 1.07×10^{-5}		3.15×10^2	7.61×10^{-1}	6.41×10^{-1}	0.00×10^0
NEUTRONS PER KT		2.70×10^{23}	3.38×10^{23}	1.95×10^{23}	1.77×10^{24}

Table 8.6. Weapon Gamma-Ray Output.

WEAPON TYPE	TOTAL GAMMA-RAY ENERGY [a], (MeV/KT)	AVERAGE GAMMA-RAY ENERGY (MeV)	PEAK GAMMA-RAY OUTPUT RATE [a, b] (MeV/nsec-KT)
3	9.80×10^{22}	1.50	4.92×10^{21}
5	1.04×10^{23}	1.61	5.22×10^{21}
8	$3.55 \times 10^{23} \times W^{-0.29}$	1.63	$1.79 \times 10^{22} \times W^{-0.29}$
13	6.70×10^{23}	2.00	3.37×10^{22}

Notes: a - W is yield in kilotons.

b - Illustrative values based on a hypothetical prompt gamma-ray pulse duration of 20 nsec.

8.2.3 Radiation Transport.

8.2.3.1 Uniform Air. In uniform air, the uncollided particle fluence ϕ from a point source is:

$$\phi (R) = N_o e^{-k\rho R}/4\pi R^2 , \tag{8.1}$$

where k is the mass attenuation coefficient (cm²/g), R is the radial distance from the source, and N_o is the total number of particles emitted by the point source.

The equivalent expression in terms of energy is:

$$D_p = \psi_p W A e^{-K\rho R}/4\pi R^2 , \tag{8.1a}$$

where D_p is the dose, ψ_p the total energy (MeV/KT), W the yield (KT), A is the unitless coefficient 0.523, and ρ is the air density (g/cm²). The uncollided fluence may be enhanced by secondary scatterings which redirect initially scattered particles back towards the target. This buildup effect is approximated by a second exponential term used for R ≥ 100 meters:

$$D_p = [\psi_p W/4\pi R^2][(A e^{-K_1\rho R})(1+B e^{-K_2\rho R})][kerma] , \tag{8.2}$$

where B is the unitless coefficient 1.356 (for gamma rays), K_1 is the effective mass attenuation coefficient (cm²/g), having a value of 0.0371 for the collided and uncollided components, K_2 is the coefficient in the buildup factor exponent (cm²/g) having a value of -0.0061, and (kerma) is the effective kerma factor for prompt gamma rays [obtainable from Table 8.3, as a function of photon

Table 8.9. Summary of Figures in Section 8.3.

Variable Parameter	Fixed Parameter(s)	Figure Numbers
Weapon Types	European soil	8.26, 8.27, 8.28, 8.29
Soil Types	Boosted fission weapon	8.30, 8.31, 8.32, 8.33
Soil Types	Enhanced radiation (ER)	8.34, 8.35, 8.36, 8.37, 8.38
Ground Moisture	Boosted fission weapon	8.24
Soil Constituents	Boosted fission weapon (European soil)	8.23
Detector Altitude	Boosted fission weapon (European soil)	8.25

8.3.2 Important Parameters of Ground Activation.

8.3.2.1 Weapon Types. The activation dose model used provides data for five generic weapon types: pure fission, boosted fission, thermonuclear, low-yield enhanced radiation (ER), and high-yield, with the first three generally quite similar and the ER weapons producing significantly higher levels of activation because of their large yield of high-energy neutrons. These five types encompass the range of neutron spectra expected to be important for ground activation. Table 8.10 gives the HOBs used to produce the data in Section 8.3, the HOB range over which the results should be reliable, and the general yield range to which the data apply. In general, the data presented have been normalized to 1 KT, and may be scaled directly with yield within this range. The dose for other HOBs than the data HOB, but within the HOB range, may be found by maintaining a constant slant range for use in the HOB figures.

Table 8.10. Height of Burst and Yield Range for Generic Device Types.

Device Type	Data HOB (meters)	HOB Range (meters)	Yield Range (KT)
Enhanced Radiation (ER) (13)			
Low Yield	75	50 - 100	1 - 5
High Yield	200	100 - 300	5 - 15
Thermonuclear (8)	200	150 - 500	10 - 500
Boosted Fission (5)	160	60 - 300	1 - 20
Fission (3)	150	60 - 300	0.5 - 15

8.3.2.2 Soil Types. The activation model used 35 target nuclides, 90 different reaction cross sections, and 33 radioactive product nuclides. The dose rate is usually dominated by one or two radioactive nuclides whose half-lives are of the order of the time since the detonation. Table 8.11 lists these nuclides, their half-lives, and the target nuclides and neutron reactions which lead to them.

Table 8.11. Important Radioactive Nuclides for Ground Activation Dose.

Dominant Time (hours)	Radioactive Nuclide	Half-Life (hours)	Target Nuclides — Capture Reaction	Target Nuclides — Fast Neutron Reactions
0 - 0.3	Al^{28}	0.04	Al^{27}	Si^{28}
0.3 - 3.0	Mn^{56}	2.58	Mn^{55}	Fe^{56}, Fe^{57}, Fe^{58}
3.0 - 200	Na^{24}	15.02	Na^{23}	Al^{27}
200 - 5,000	Fe^{59}	1,070.4	Fe^{58}	Co^{59}, Ni^{62}
5,000 - 40,000	Mn^{54}	7,500	Mn^{55}	Fe^{54}, Fe^{56}
> 40,000	Na^{22}	22,800	Na^{23}	

Four soil types, with varying concentrations of sodium, silicon, aluminum, manganese, and iron, are used to cover the range of activation levels that might be expected. Table 8.12 gives the composition of the critical target elements for each of these soil types. The Mojave and Dade Country types were selected to produce, respectively, reasonable upper and lower limits of activation. The other two types

will give nominal levels of activation. Figure 8.23 shows the fractional contribution to the dose rate for each of the nuclides versus time after burst for European type soil.

Moisture in the soil can reduce the activation by as much as 50 percent. This is illustrated in Figure 8.24 showing the 1-hour dose rate for a boosted fission device over European soil of varying moisture content up to 28 percent. Similar results are obtained for other weapon types, including ERs. All other data in Section 8.3 are for dry soils.

8.3.2.3 Detector Altitude. The activation dose level varies with the height of the detector above the ground plan. This variation is caused by the change in the slant penetration from the soil source of radiation through ground to the air and by additional air attenuation. This effect is illustrated in Figure 8.25 for the boosted-fission device and European soil. All other data in this section are for a detector height of 1.5 meters.

8.3.3 Graphical Calculational Database.

8.3.3.1. Variation with Weapon Type for Nominal (European) Soil. Figures 8.26 through 8.29 provide ground-activation dose and dose-rate data for the five weapon types for nominal European type soils. The HOB and yield ranges appropriate for these curves have been given in Table 8.10. Figures 8.26 and 8.27 are the dose rate and dose, respectively, versus slant range at 1-hour time. Figure 8.28 gives the dose rate at ground zero versus time for the five weapon types. Figure 8.29 gives the cumulative fractional dose at ground zero versus entry time after the burst for the five weapon types. Table 8.13 gives the total (integral) dose in European soil at ground zero, that is, the time-integrals of the dose-rate curves from Figure 8.28.

Table 8.12. Critical Target Composition of Soil Types.

Soil Type	Percent by Weight				
	Sodium	Silicon	Aluminum	Maganese	Iron
Mojave	3.30	23.5	9.57	0.14	7.31
European	1.39	28.3	4.05	0.12	1.98
Nevada Area 7	0.80	25.3	7.70	0.07	1.52
Dade County	0.12	45.4	0.03	0.01	0.06
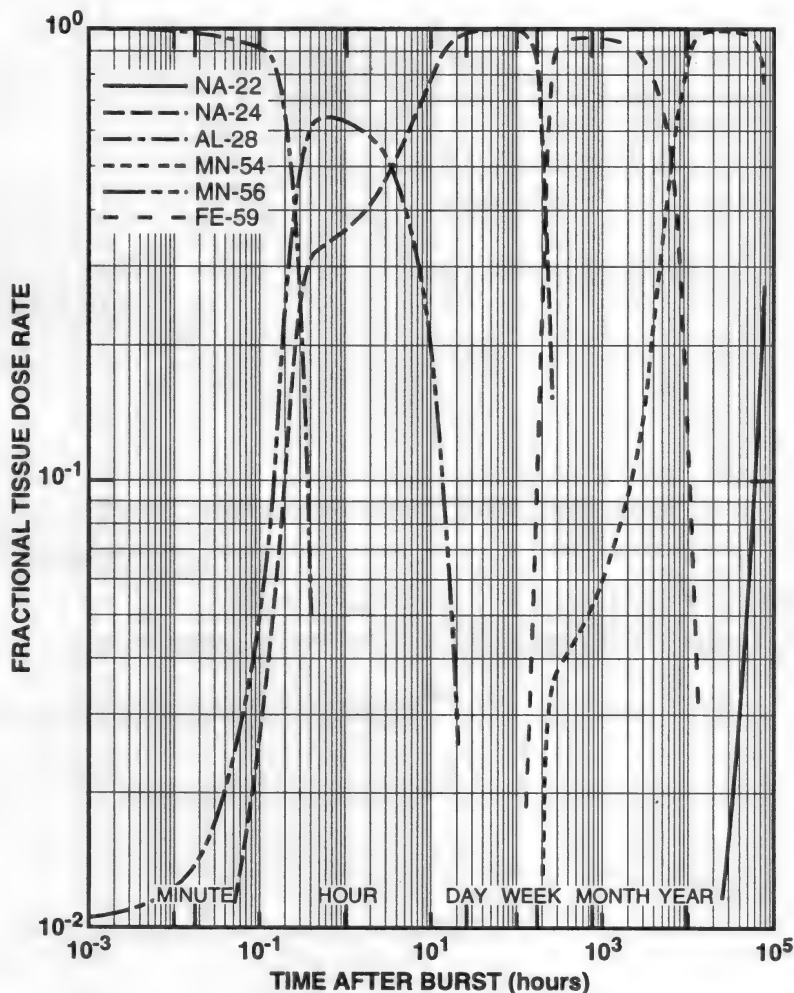
Figure 8.23. Fraction of Total Gamma-Ray Dose Rate at Ground Zero Versus Time From the Activity of Various Radioactive Nuclides Produced in European Soil by Neutrons From a Boosted-Fission Device.

To find the dose rate for some slant range (not ground zero) at a particular time, the dose rate at ground zero at the appropriate time (Figure 8.28) is multiplied by the ratio of the total dose at the appropriate slant range (Figure 8.27) to the total dose at ground zero (Table 8.13). Gamma-ray dose at a given slant range for a particular stay period can be found by correcting the data of Figure 8.27 (dose for an infinite stay time starting at time zero) by a factor which is the fractional dose at time of entry minus that at time of departure (from Figure 8.29).

Figure 8.26. Gamma-Ray Dose Rate per Kiloton Yield at 1 hour Versus Slant Range From Neutron Activation of European Soil for Various Nuclear Weapon Types.
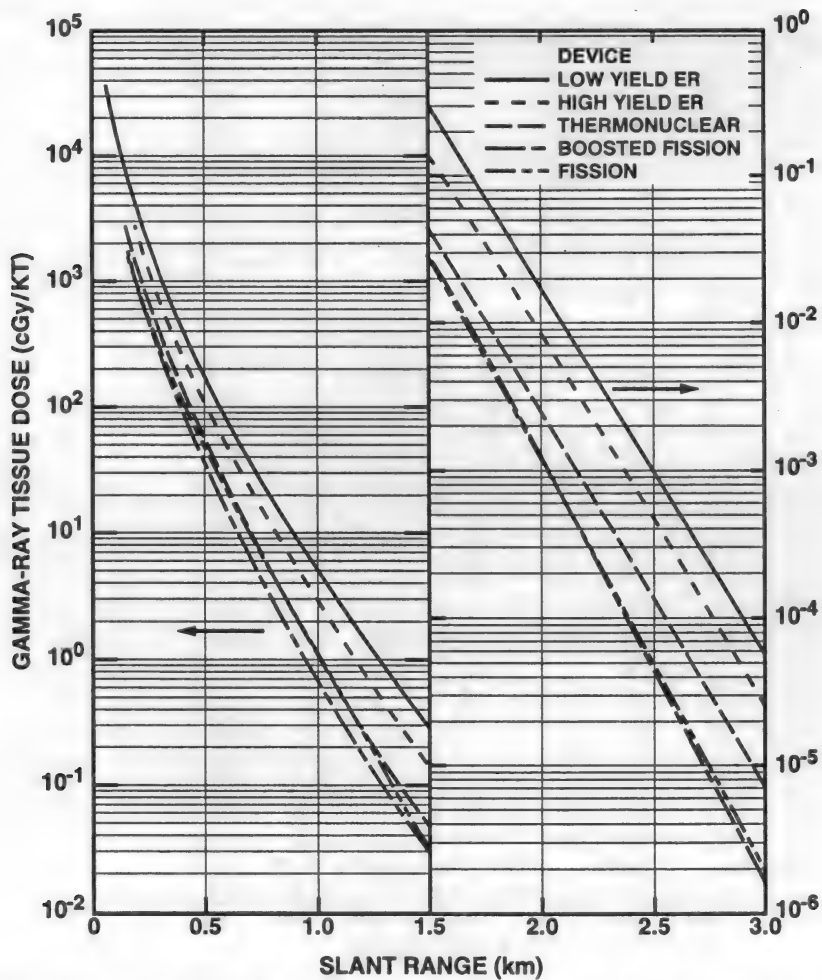
Figure 8.27. Total Gamma-Ray Dose per Kiloton Yield Versus Slant Range From Neutron Activation of European Soil for Various Nuclear Weapon Types.
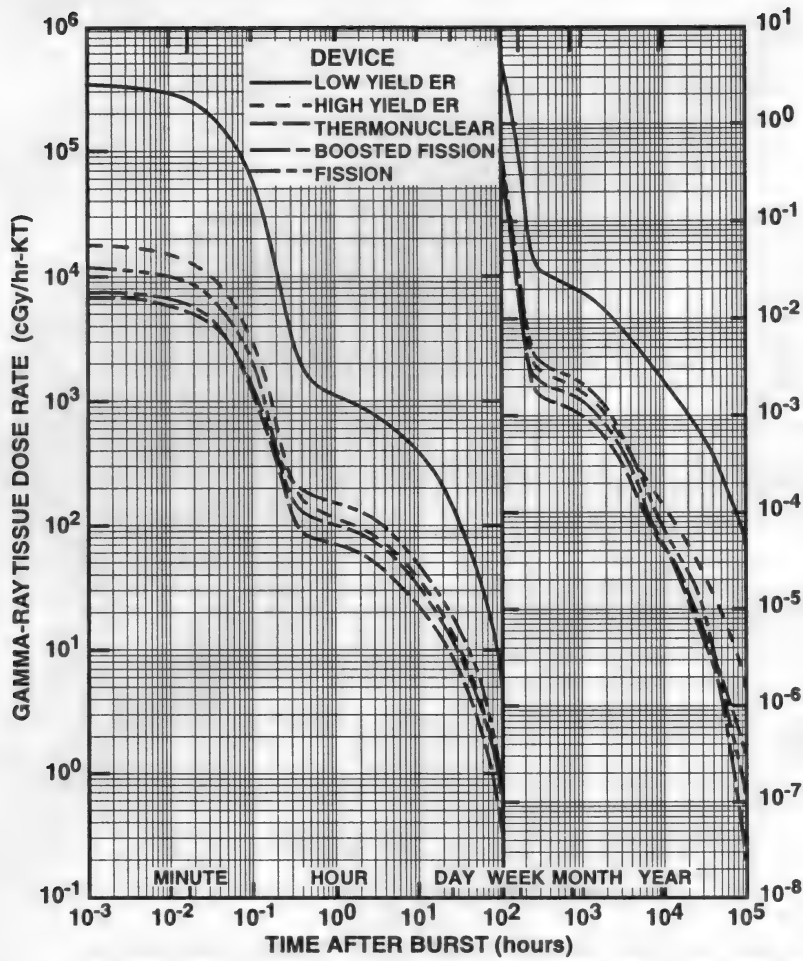
Figure 8.28. Gamma-Ray Dose Rate per Kiloton Yield at Ground Zero Versus Time After Burst From Neutron Activation of European Soil for Various Nuclear Weapon Types.
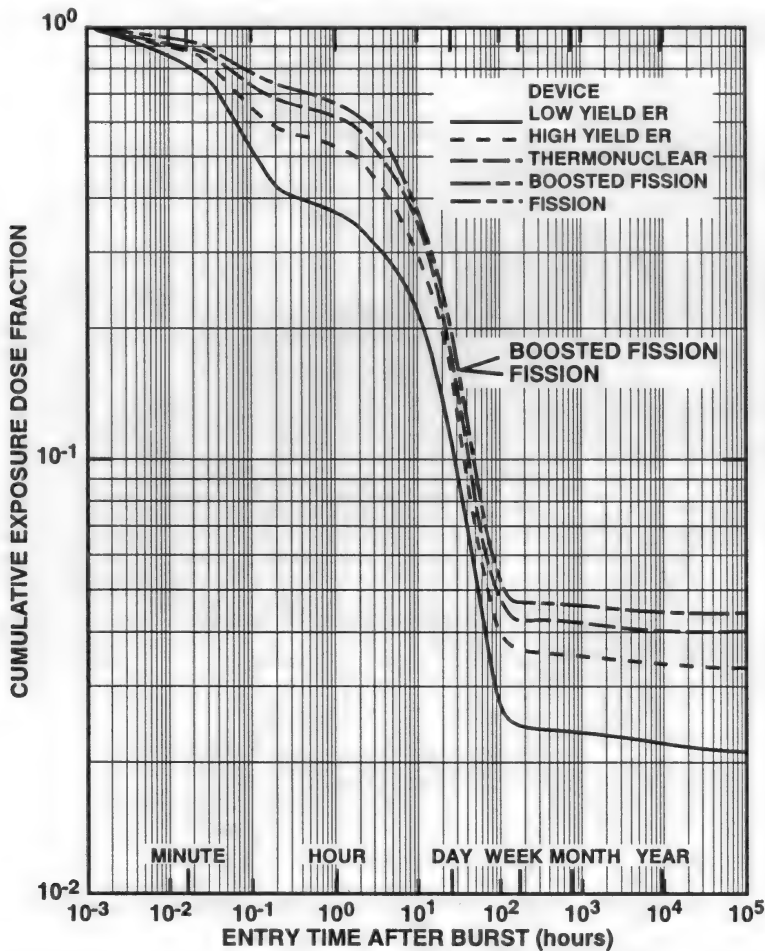
Figure 8.29. Cumulative Gamma-Ray Dose Fraction at Ground Zero Versus Entry Time After Burst From Neutron Activation of European Soil for Various Nuclear Weapon Types.
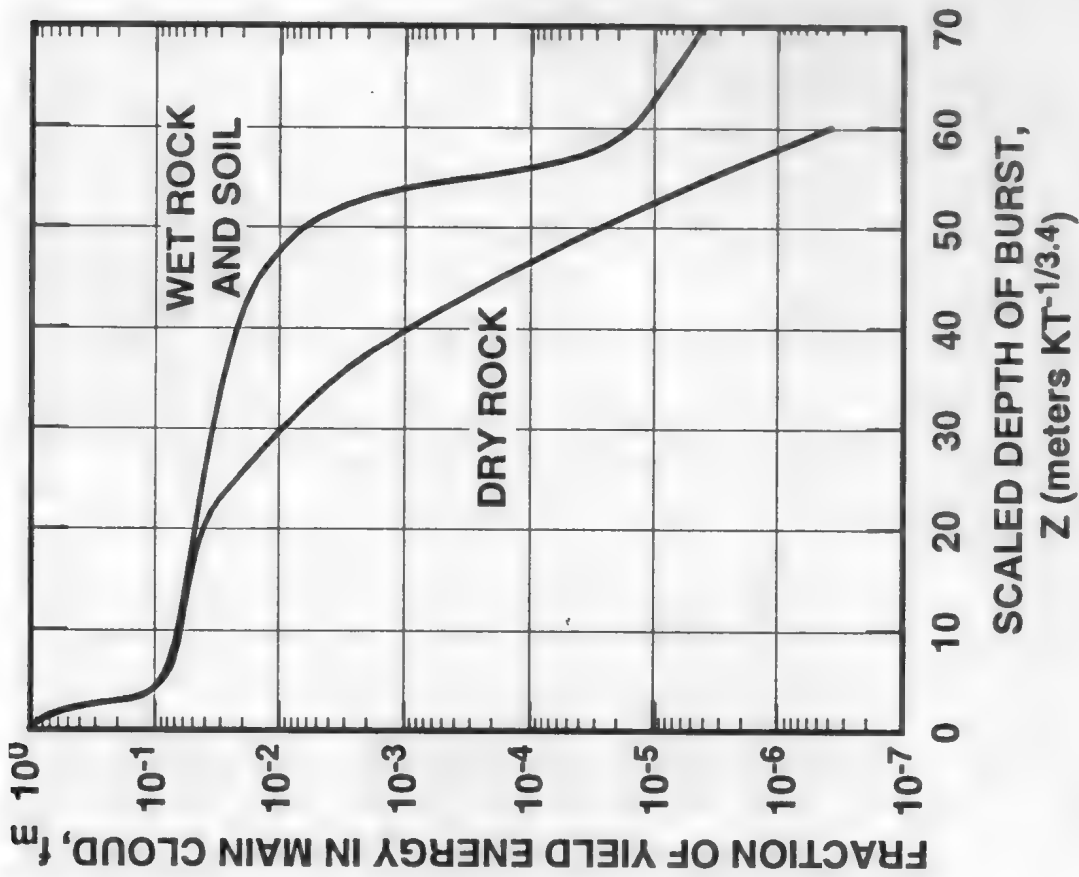
Figure 8.45. Fraction in Main Cloud.
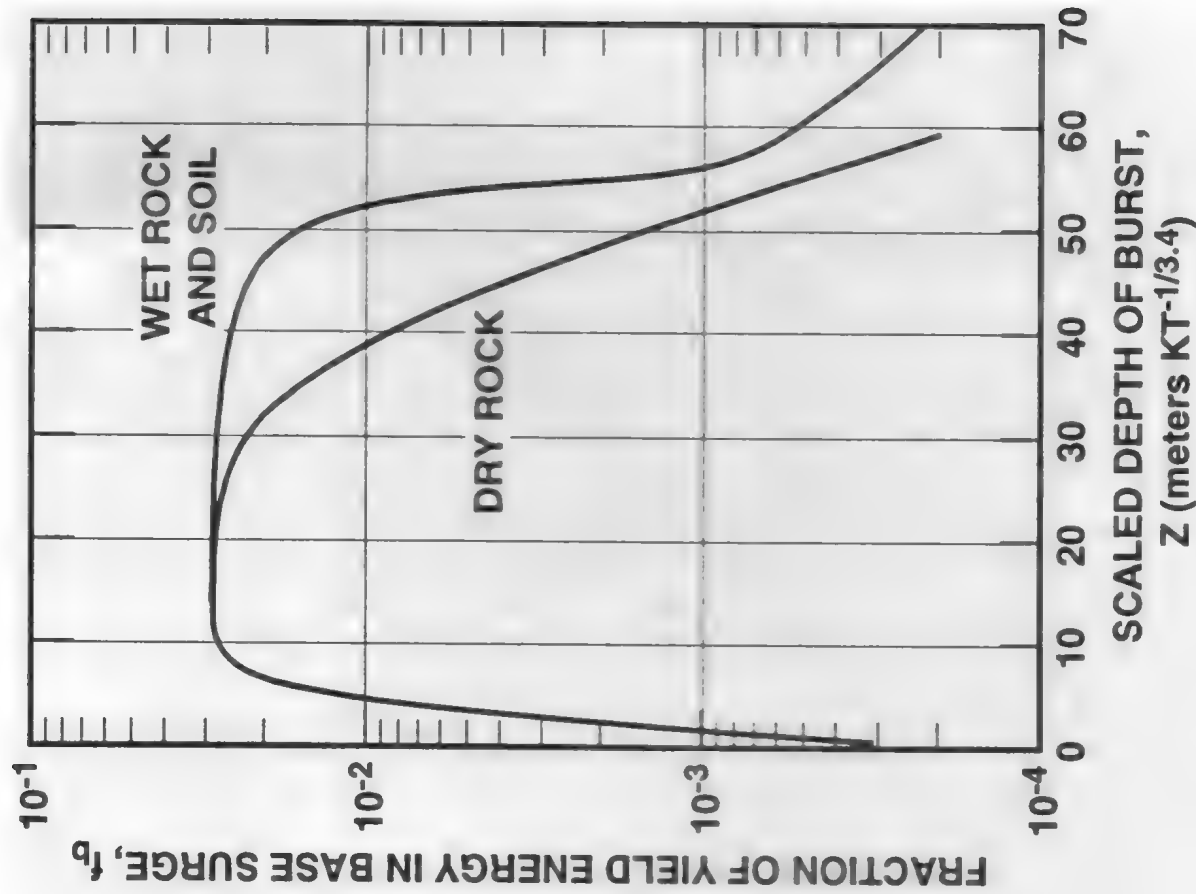
Figure 8.46. Fraction in Base Surge.

Fraction of Energy Yield from a Subsurface Burst Versus Scaled Depth of Burst: Wet Rock has a Moisture Content of > 1 Percent.

4. NUCLEAR PARTICULATE CLOUDS

4.1 Introduction. The particulates in nuclear clouds are combinations of (1) surface dust raised by the blast wave passage over the ground, (2) crater ejecta lofted by the rising fireball, and (3) condensed water in several forms arising from the condensation of moisture in the air which is cooled as it rises and expands. The research database consists of atmospheric test observations, HE testing, and hydrocode modeling. The atmospheric test data are generally limited to photographic measurements of cloud dimensions, while quantitative data on internal cloud dynamics and particulate sizes as a function of time and location in the cloud are essentially nonexistent. Thus the quantitative data in this handbook are limited primarily to algebraic expressions for some of the macroscopic features of clouds such as dimensions and total particulate entrainment.

Detailed characterization of the spatial and temporal effects in the particulate environments requires the use of hydrocodes which model the physical processes involved and are adjusted to be consistent with the macroscopic features of experimental data. The DICE and TASS linked hydrocodes are the primary models used to calculate the detailed characteristics of the lofted dust/ice concentrations and distributions of solid material by particle size as functions of altitude, radius, and time. *EM-1* contains the results of a relatively small number of such calculations, which are tutorial and illustrative of trends but do not provide the basis for further numerical analysis.

4.1.1 Dust Size Distributions. Particle size distributions (PSDs) are a function of geology, terrain, and meteorology, as well as differing between ejecta and sweep-up sources. Figure 4.1 shows the currently accepted range of PSDs. The DICE/TASS calculations use power-law approximations to "incohesive soil" for the swept-up mass and "coarse alluvium" for ejecta.

4.1.2 Particulate Slip Velocities and Settling Times. The slip speed of a particle is its equilibrium settling speed (or terminal velocity) in quiet air under the influence of gravity alone. It depends on the diameter, roughness, and density of the particle, and the density ρ_g and viscosity μ of the ambient gas which change with altitude and temperature.

The density of a dust particle, ρ_d, is set at 2 g/cm^3 in the DICE/TASS calculations, and a multiplier of 1.5 times the drag coefficient approximates the enhanced drag on rough spheres. Other terms are the sphere diameter, d and the acceleration of gravity, g = 980 cm/sec^2. The slip velocity is calculated through the following equation:

$$v_T = \left(\frac{30\mu}{\rho_g d}\right)\left(-1 + \sqrt{1 + d^3 \frac{g\rho_g\rho_d}{405\mu^2}}\right). \tag{4.1}$$

Figure 4.2 shows slip velocity as a function of particle diameter at sea level and an altitude of 10 km, as calculated from Equation 4.1. Settling times as a function of particle diameter are shown in Figure 4.3. Particles in the 10- to 100-μm range require from several hours to many days to fall from nuclear cloud stabilization altitudes above 10 km. Particles larger than 1 mm, which fall out in about 10 minutes or less, will generally be retarded by the modest but sustained updrafts possible below the cloud in that period.

4.2 Simple Formulae. This section provides simple formulae for some parameters. These equations represent an effort to systematize the limited data from atmospheric nuclear tests and available calculations, but it should be recognized that the test sites are special cases of terrain and atmospheric conditions.

4.2.1 Cloud Dimensions. The most obvious parameters are the geometrical dimensions of the photographic cloud. The top of the main cloud rises to and possibly overshoots an equilibrium altitude. The yield-dependent relation of the main cloud stabilization height above the burst point is the empirical formula:

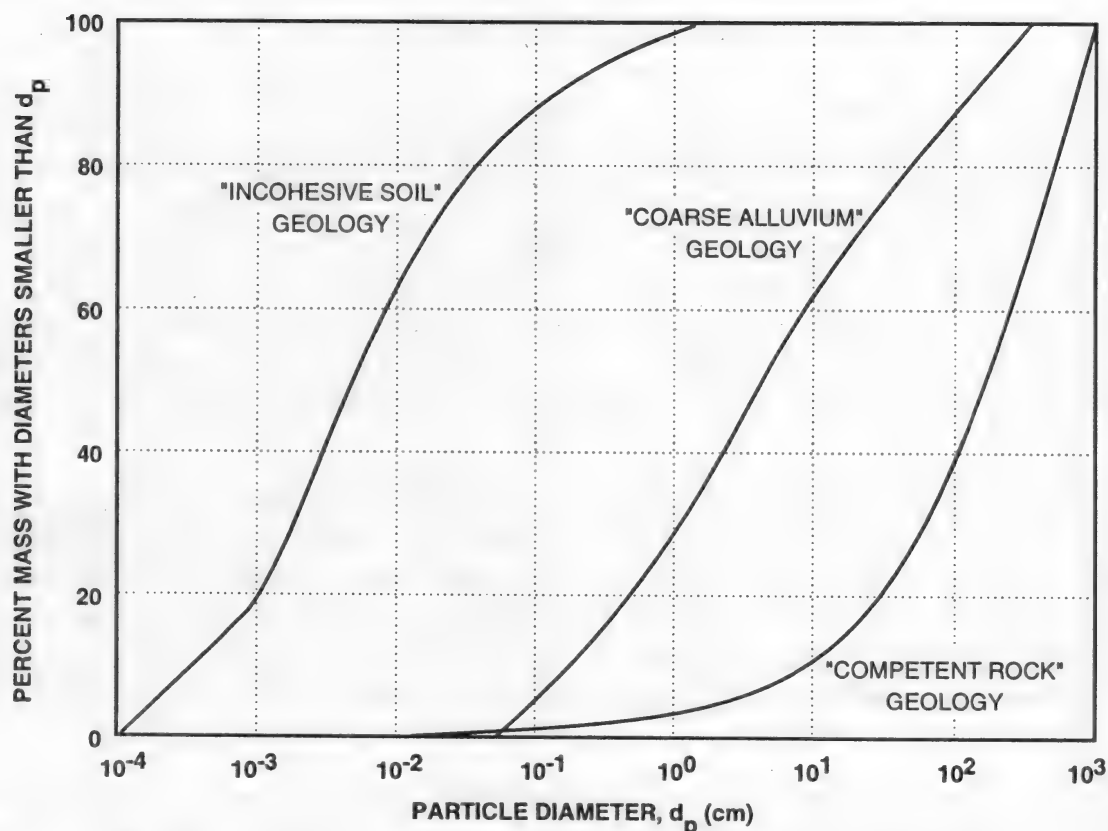$$\Delta H_{top} = 4.5 \, W^{0.22} \, (km), \tag{4.2}$$

Figure 4.1. Particle Size Distributions for a Range of Site Conditions.

where W is the yield in kilotons and ΔH_{top} is in kilometers. The stabilized bottom of the main cloud for most yields is not perfectly correlated with the top. Nevertheless, an approximate relation exists for the thickness of the main cloud at stabilization:

$$\Delta H_{thk} = 2\ W^{1/5}\ (km)\ ,\ \text{for yields greater than 2 KT.} \tag{4.3}$$

The cloud diameter is the important horizontal extent. A combined yield- and time-dependent relationship is:

$$D = 0.65\ t^{3/7}\ W^{(2 + \log t)/7}\ (km)\ , \tag{4.4}$$

with W in KT and for time $t \le 10$ minutes.

This formula is not appropriate at late time due to the dominance of the wind shear effect on the cloud width after stabilization. Also, note that low yield (< 50 KT) clouds can easily be much larger than this formula by 10 minutes after burst.

Sample Problem 4.1. Determining Cloud Dimensions. For a 100-KT burst at a height of 100 meters, find the cloud top height, thickness of main cloud, height of the main cloud bottom, and its diameter at 10 minutes after detonation.

Stabilized top rise (Eq. 4.2):	$\Delta H_{top} = 4.5(100)^{0.22} = 12.4 km$
Stablized top above ground:	$H_{top} = \Delta H_{top} + HOB = 12.4 + 0.1 = 12.5 km$
Stabilized cloud thickness (Eq. 4.3):	$\Delta H_{thk} = 2(100)^{0.2} = 5.0 km$
Height of cloud bottom:	$H_{bottom} = 12.5 - 5.0 = 7.5 km$
Main cloud diameter (Eq. 4.4):	$D = 0.65(10)^{3/7}(100)^{(2+\log t)/7} = 12.5 km$

4.2.2 Dust Pedestal. The pedestal refers to the slowly varying sweep-up layer that develops by about 1 s/KT$^{1/3}$. The Scaled Maximum Height (SMH) of the dust pedestal (at the scaled time of approximately 1 s/KT$^{1/3}$) is:

$$SMH = 525\ SHOB^{-0.865}\ (m/KT^{1/3})\ , \tag{4.5}$$
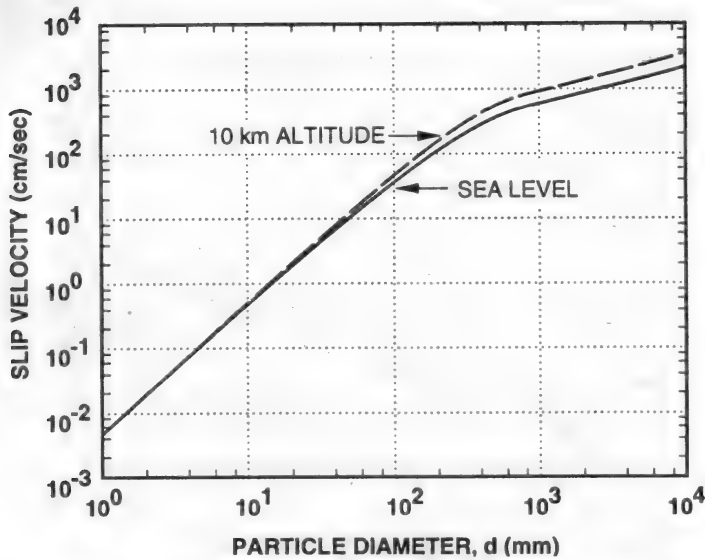
Figure 4.2. Slip Velocity Versus Diameter for Rough Dust Particles at Sea Level and 10 km Altitude.
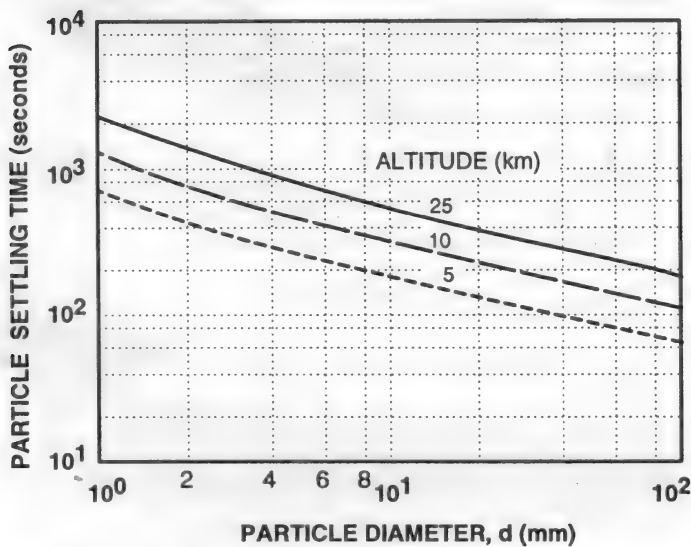
Figure 4.3a. Particle Settling Time(s) in Still Air Versus Large Particle Diameter (mm).
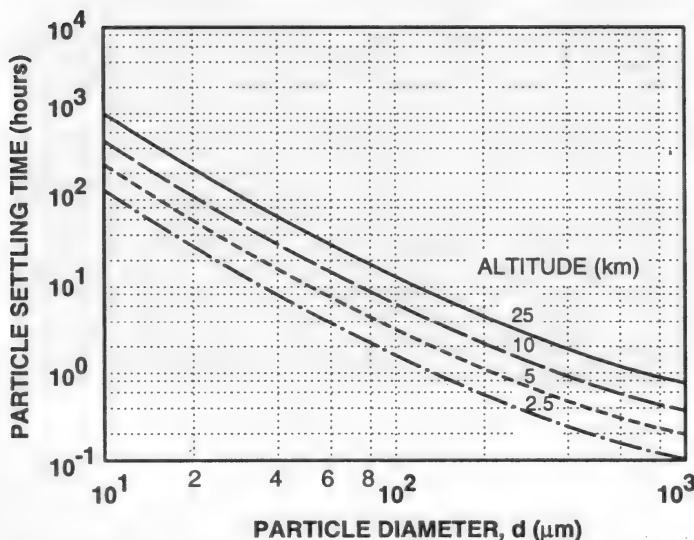
Figure 4.3b. Particle Settling Time(s) in Still Air Versus Small Particle Diameter (micron).

where the scaled height of burst (SHOB) is restricted to >10 m/KT$^{1/3}$. The time-dependent algorithm is shown in Figure 4.4.

The SMH occurs at the Scaled Ground Range for Maximum Height (SGRMH) (m/KT$^{1/3}$) of:

$$SGRMH = 120 + 2 \ (SHOB) \ (m/KT^{1/3}) , \tag{4.6}$$

with SHOB in m/KT$^{1/3}$ at t ~ 1 sec/KT$^{1/3}$. The time-dependent fit is shown in Figure 4.5.

The Maximum Scaled Ground Range (MSGR) of the dust pedestal is variable due to the thermal layer variations. The time-dependent fit is shown in Figure 4.6. The empirical results are that the MSGR is:

$$MSGR = 150 + 2.5 \ (SHOB) \ (m/KT^{1/3}) ,$$
$$\text{for SHOB} < 68 \ m/KT^{1/3}, \tag{4.7a}$$

$$\text{and MSGR} = 320 \ m/KT^{1/3}$$
$$\text{for SHOB} > 68 \ m/KT^{1/3}. \tag{4.7b}$$

Note that there is also a low-lying dust layer extending on out to about 1,000 m/KT$^{1/3}$.

4.2.3 Dust Mass Loading.

Surface Bursts (SHOB < 5 ft/KT$^{1/3}$). The collected and analyzed soil and saltwater particles provide estimates of the lofted mass in nuclear clouds. The empirical relation from combining the soil and saltwater data for scaled mass in stabilized surface burst clouds is:

$$M_{SB}/W = 0.62 \ W^{-0.11} , \tag{4.8a}$$

where W is the yield in KT and M_{SB} is in KT $= 10^9$ grams, or

$$M_{SB}/W = 0.29 \ W^{-0.11} , \tag{4.8b}$$

where W is in MT and M_{SB} is in Mt $= 10^{12}$ g.

Airbursts (SHOB $\geq$ 5 ft/KT$^{1/3}$). The experimental mass loading data have large scatter. DICE/TASS calculations have been used with these experimental data to generate the following approximated main cloud mass loading relationship with SHOB.

$$M/W(KT/KT) = 0.25 \ exp(-SHOB/75) + 0.04(1-SHOB/800) \tag{4.9a}$$
$$\text{for } 5 \leq SHOB \leq 800 \ ft/KT^{1/3}, \text{ and}$$

$$M/W = 0 \text{ for SHOB} > 800 \ ft/KT^{1/3} . \tag{4.9b}$$
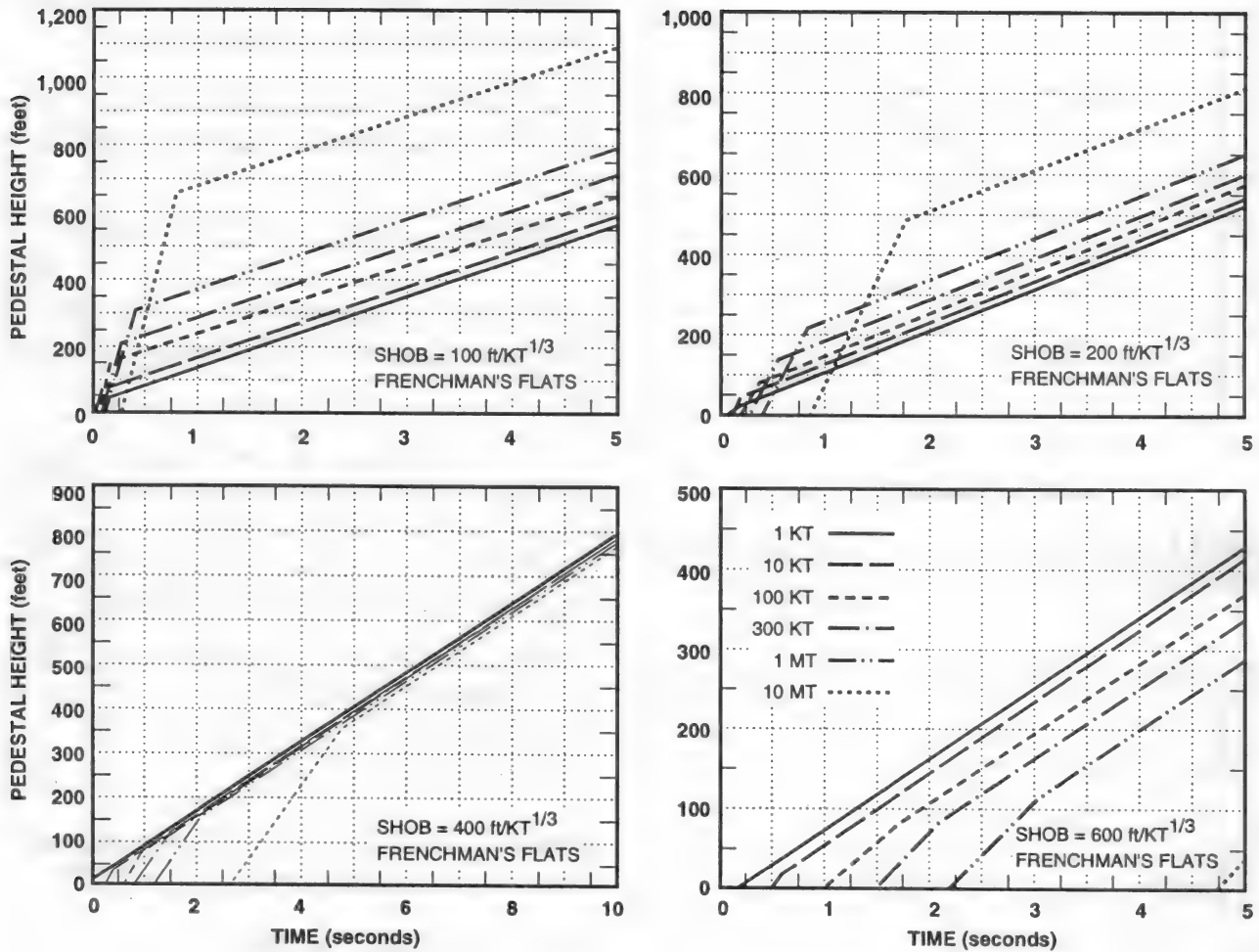
Figure 4.4. Maximum Pedestal Height Versus Time for Various SHOBs.

This relationship tends to be on the high side of the data and calculations. The uncertainties are estimated to be a factor of 3 higher or a factor of 20 lower.

Sample Problem 4.2. Determining Dust Pedestal Dimensions.

For a 100-KT burst at a height of 200 feet, find the dust pedestal maximum height, ground range for maximum height, and the maximum ground range at 1 scaled second after detonation.

Scaled height of burst (Eq. 2.10):	$SHOB = (200) / (100)^{1/3} = 43.1$ ft/KT$^{1/3}$=13.1 m/KT$^{1/3}$
Pedestal scaled maximum height (Eq. 4.5):	$SMH = (525)(13.1)^{-0.865} = 56.6$ m/KT$^{1/3}$
Pedestal maximum height:	$MH = 56.6(100)^{1/3} = 263$ m $= 862$ ft
Scaled GR at maximum height (Eq. 4.6):	$SGRMH = 120 + 2(13.1) = 146.3$ m/KT$^{1/3}$
Ground range at maximum height:	$GRMH = 146.3(100)^{1/3} = 679$ m $= 2,227$ ft
Maximum scaled GR (Eq. 4.7a):	$MSGR = 150 + 2.5(13.1) = 183$ m/KT$^{1/3}$
Maximum ground range:	$MGR = 183(100)^{1/3} = 849$ m $= 2,784$ ft
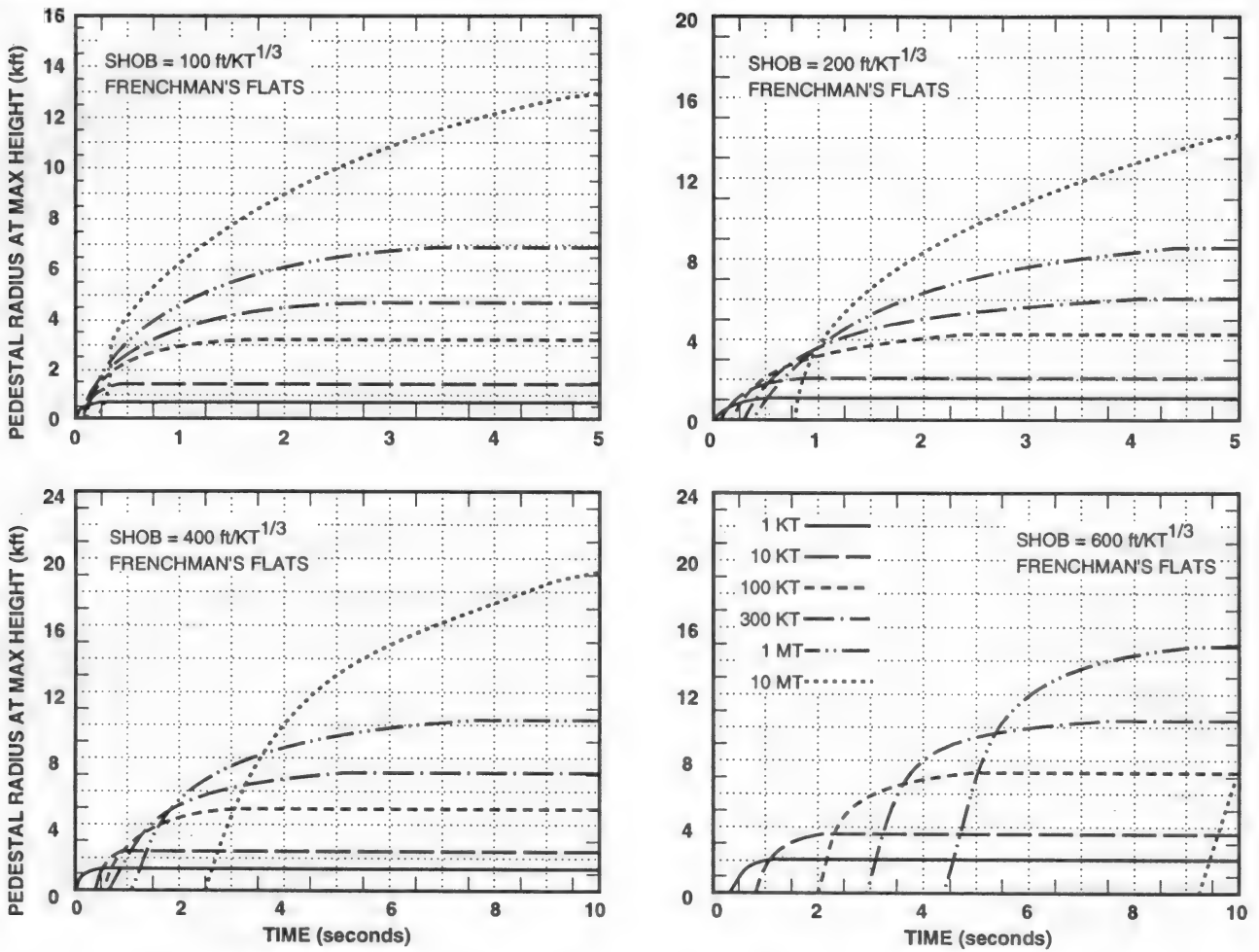
Figure 4.5. Radius at Maximum Height of Pedestal Versus Time for Various SHOBs.
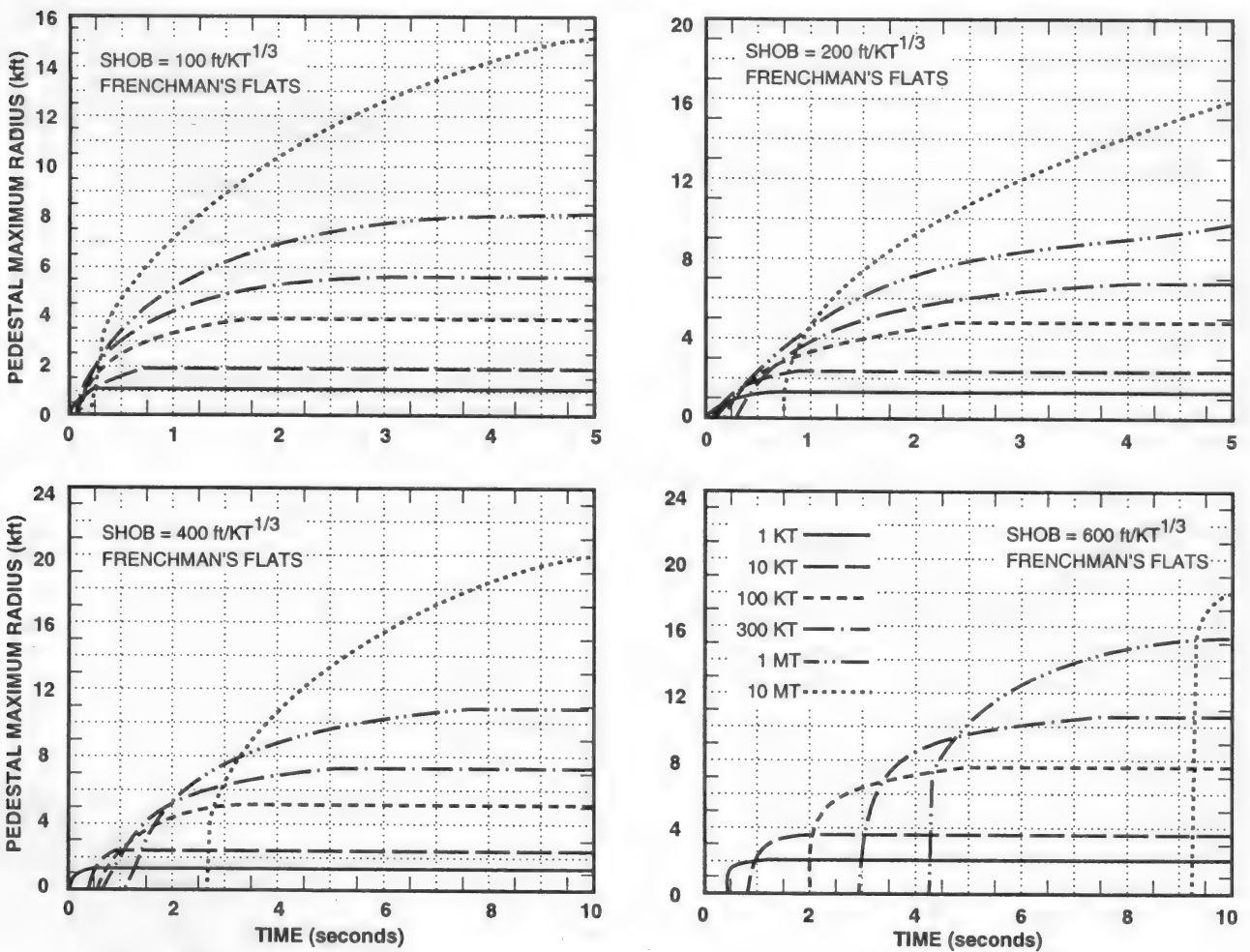
Figure 4.6. Maximum Radius of Pedestal Versus Time for Various SHOBs.
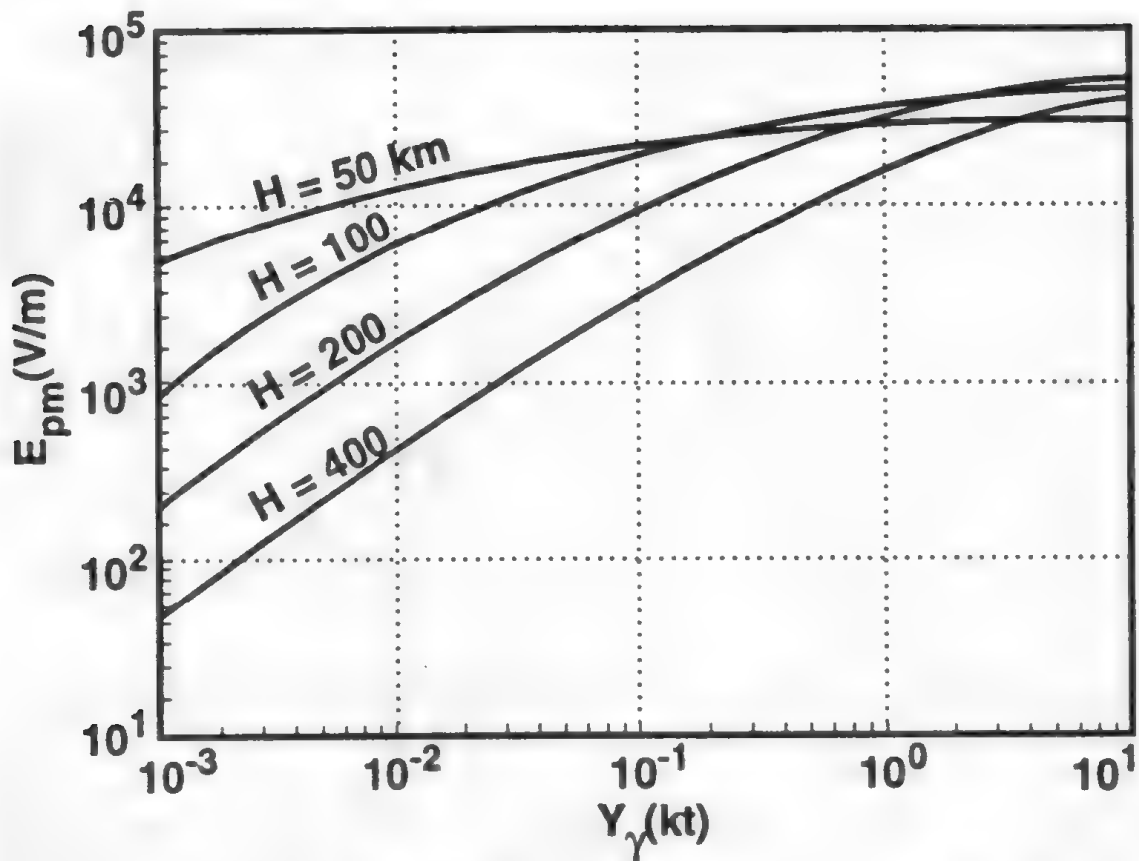
Figure 10.4. Maximum Estimated Peak
Electric Field Versus Gamma Yield for
Various Heights of Burst.
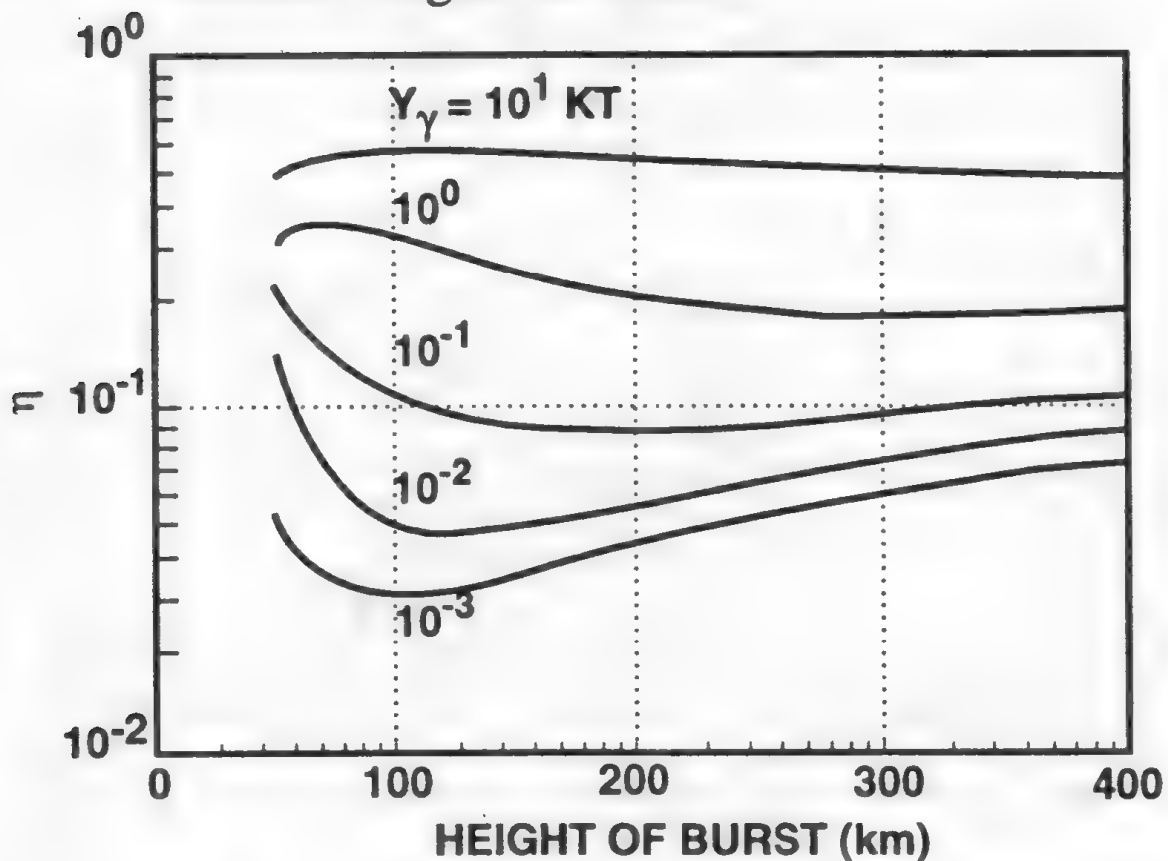
Figure 10.5. η Versus Height of Burst
for Various Gamma Yields.
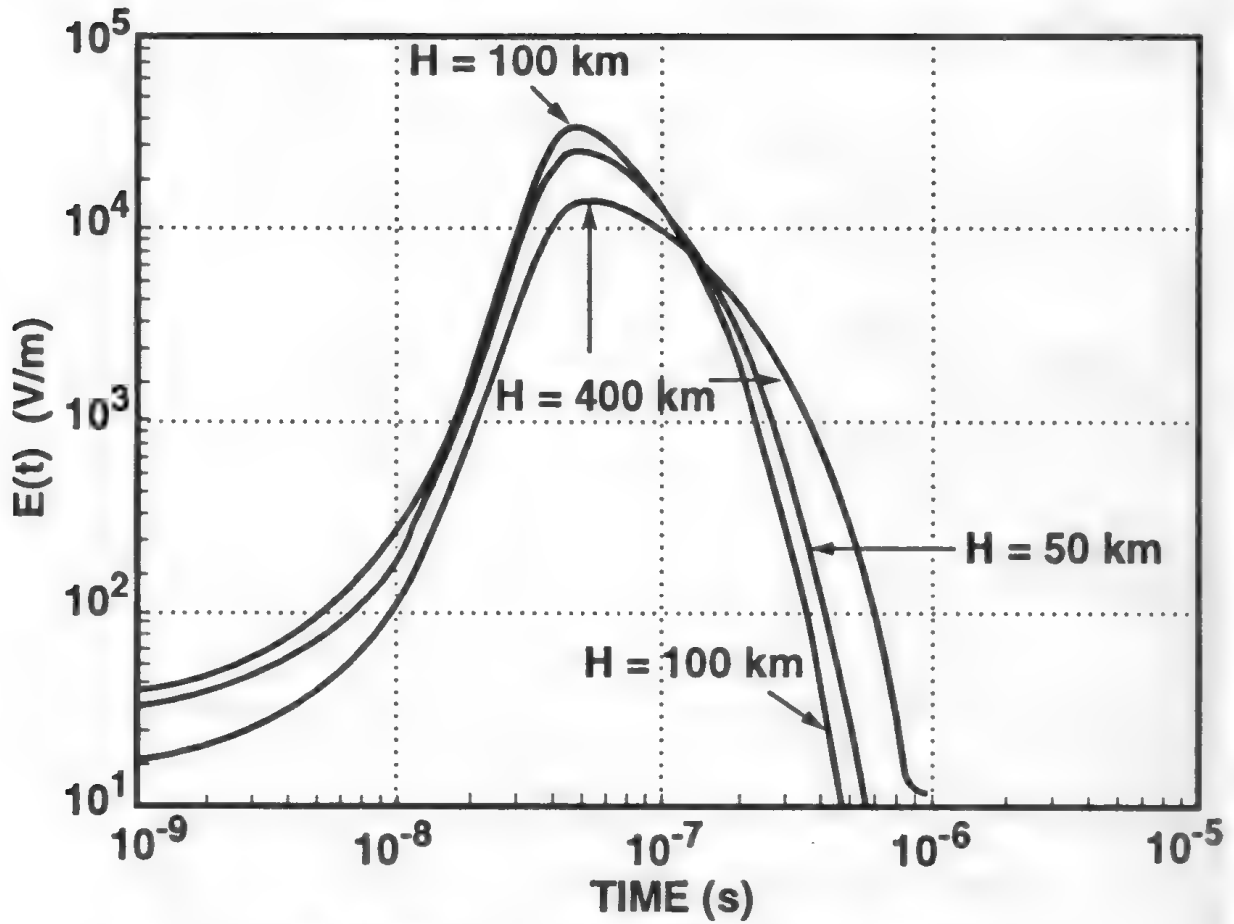
Figure 10.6. Electric Field Versus Time for $Y_\gamma = 1$ KT for Various Heights of Burst.
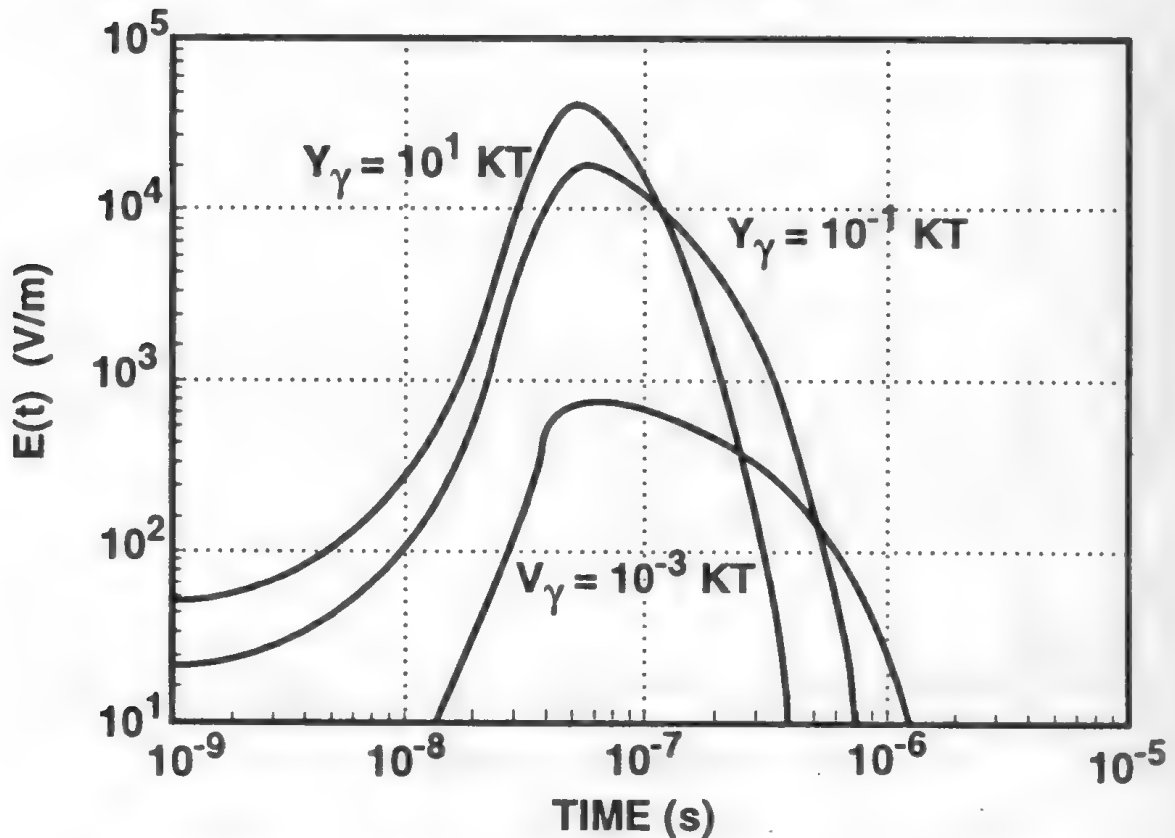
Figure 10.7. Electric Field Versus Time for Various Gamma Yields at 100 km
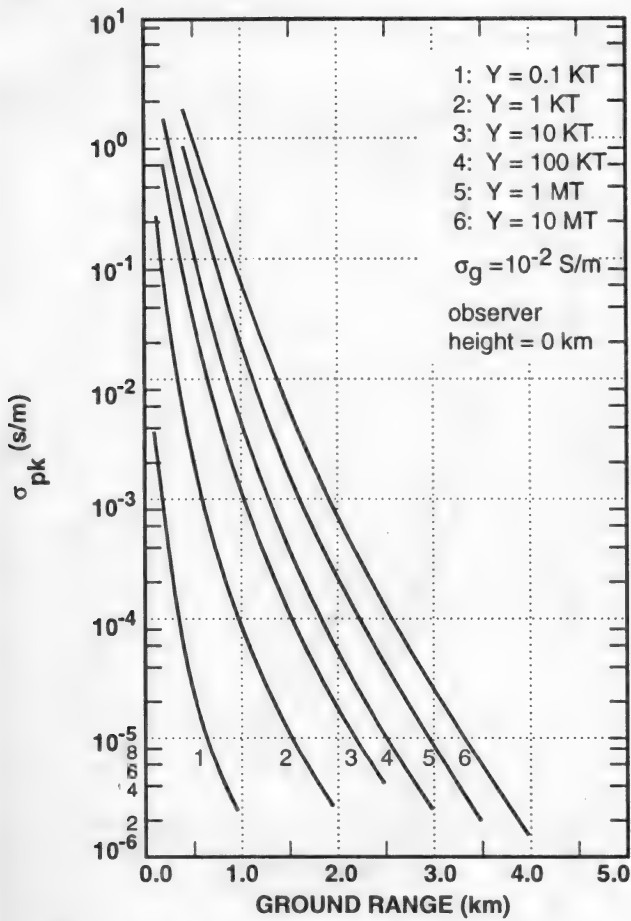
Figure 10.13. Variation of Peak Air Conductivities with Range from a Surface Burst for Various Total Yields.
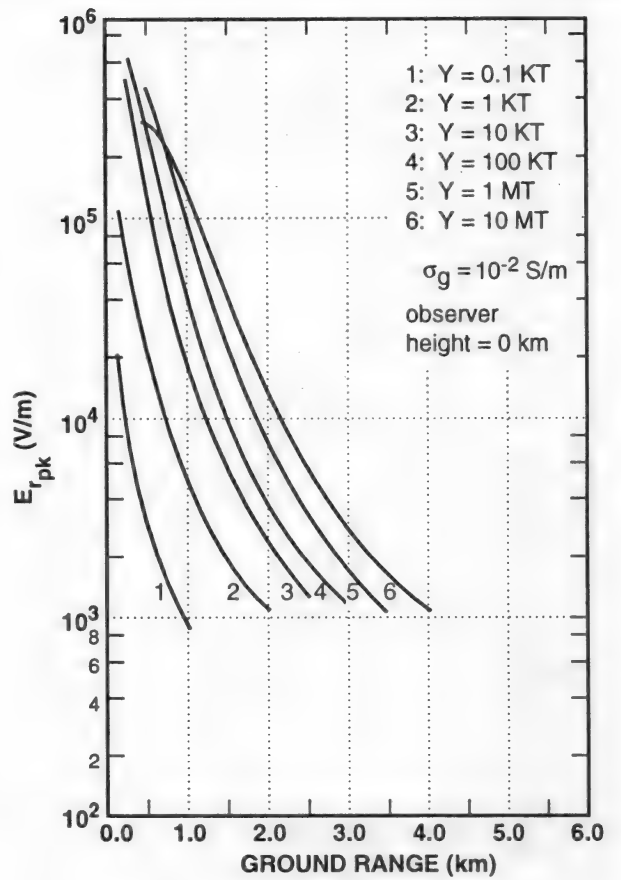
Figure 10.14. Variation of Peak Radial Electric Fields with Range from a Surface Burst for Various Total Yields.
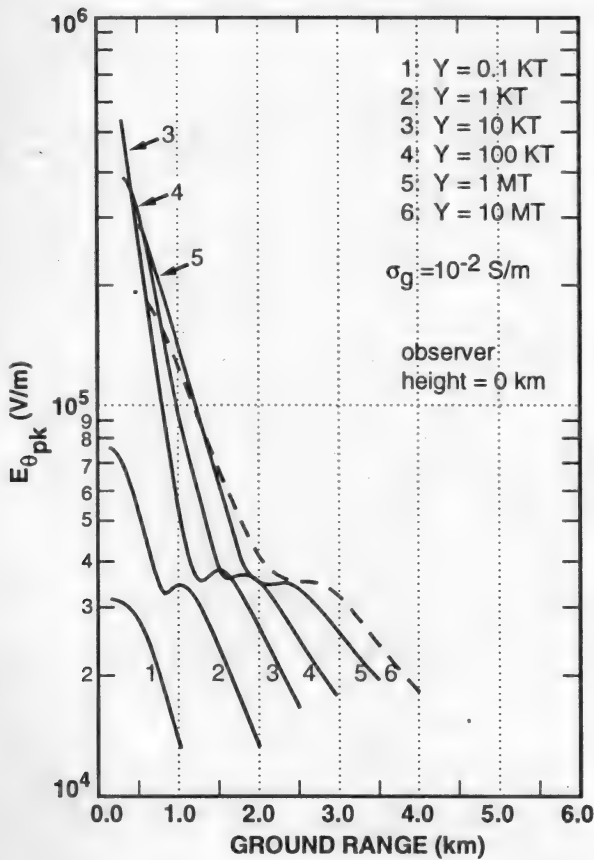
Figure 10.15. Variation of Peak Theta Electric Fields with a Surface Burst for Various Total Yields.
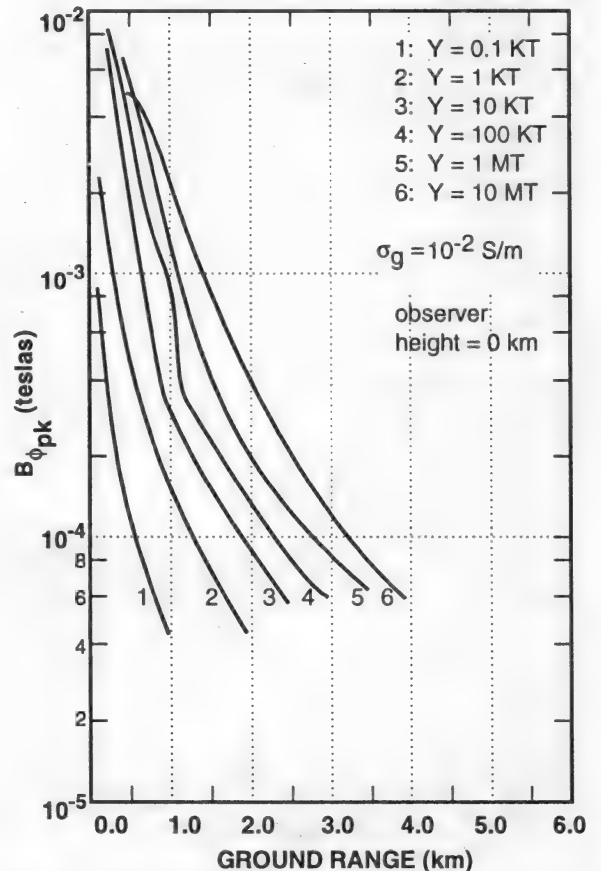
Figure 10.16. Variation of Peak Phi Magnetic Flux Densities with Range from a Surface Burst for Various Total Yields.
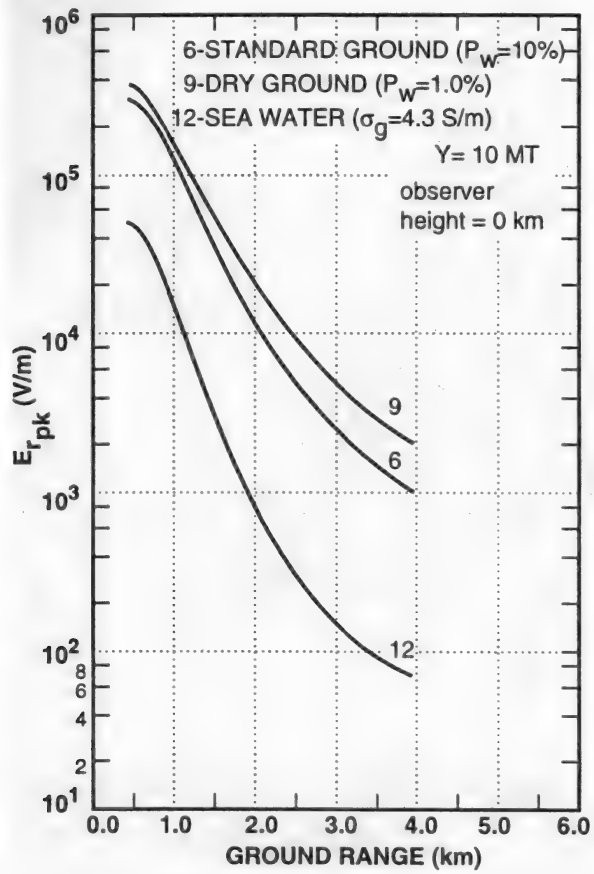
Figure 10.17. Variation of Peak Radial Electric Fields with Range from a Surface Burst for Different Ground Characteristics.
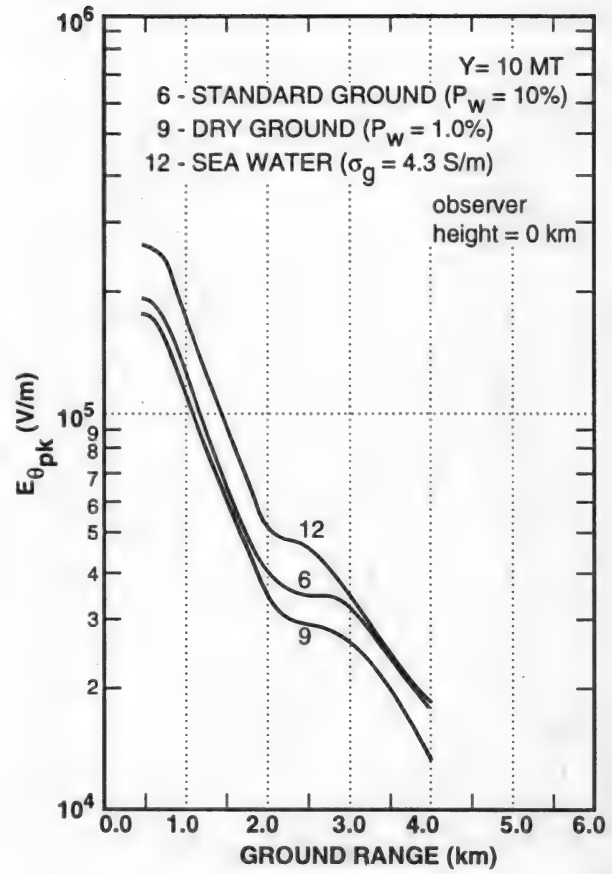
Figure 10.18. Variation of Peak Theta Electric Fields with Range from a Surface Burst for Different Ground Characteristics.
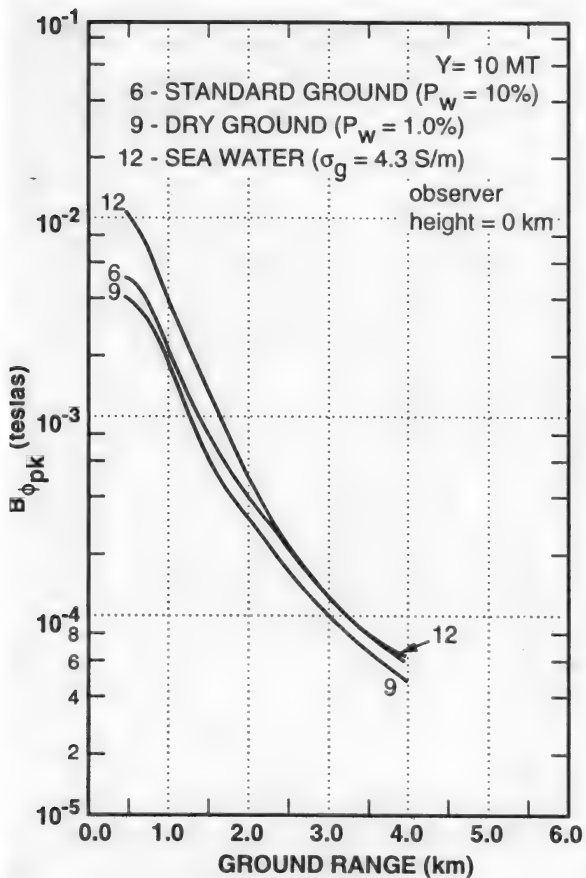
Figure 10.19. Variation of Peak Phi Magnetic Flux Densities with Range from a Surface Burst for Different Ground Characteristics.
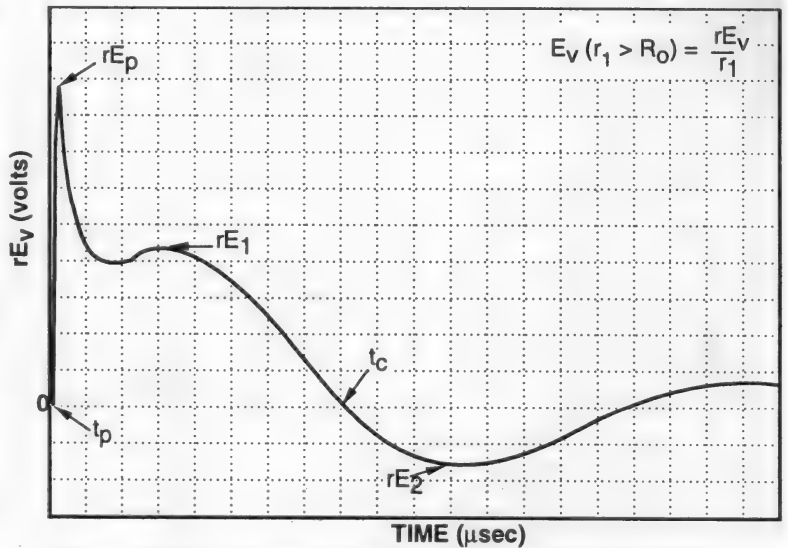
Figure 10.20. Generic Radiated Ground-Burst EMP Waveform.

6. THERMAL RADIATION PHENOMENA

6.1 Introduction. The term "thermal radiation" is conventionally restricted to that radiation emitted by the fireball, specifically excluding the early x-ray emission that is, technically, also "thermal". The fireball thermal emission typically takes place over a period of seconds, with most of the energy in the wavelength region between 0.3 μm and 4.0 μm. The energy delivered in the thermal pulse is usually specified in terms of thermal fluence, which is the energy per unit area incident on a target surface (calories per square centimeter). The thermal fluence is:

$$Q = 100 \ WfTg/ \ 4\pi R_S^2 \ \text{cal/cm}^2 , \tag{6.1}$$

where:

R_S = slant range (km) from the source $\qquad 4\pi R_S^2$ = spherical area of distribution
f = thermal fraction $\qquad\qquad\qquad\qquad$ W = yield (KT)
T = transmittance $\qquad\qquad\qquad\qquad\qquad$ g = geometry factor (including extended
$\quad$ (including attenuation and albedo) $\qquad\qquad$ source and target orientation).

Equivalent expressions are:

$$Q = 7.96 \ WfTg/R_S^2(km) \ \text{cal/cm}^2 \quad \text{or} \quad Q = 85.7 \ WfTg/R_S^2(kft) \ \text{cal/cm}^2 .$$

The rate at which thermal energy is emitted is the thermal flux (cal/sec). Bursts at low and intermediate altitudes typically emit thermal energy in two peaks, the first in the millisecond and the second in the second time-scale. Figure 6.1 illustrates these two peaks for a 1-KT, low-altitude burst, emphasizing the variability in the first peak resulting from uncertainties in non-equilibrium absorption. Since less than 1 percent of the thermal energy is contained in this first pulse, it has generally been excluded from the material presented in this chapter.
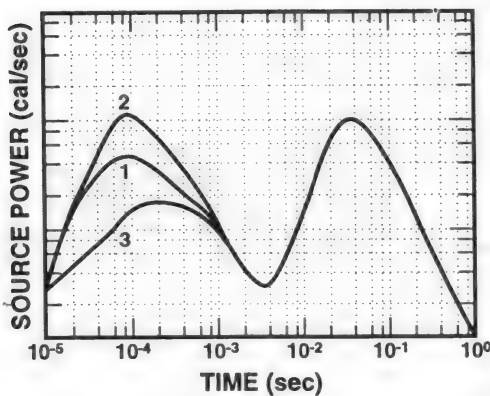

Figure 6.1. Illustrative Fireball Thermal Power Versus Time for a 1-KT, Low Altitude Nuclear Explosion, Showing Variability of the First Pulse.

6.2 Thermal Radiation Source Characteristics. Data in this section are taken from the RECIPE fireball radiation model, an engineering model developed to reproduce the results of the RHGEN first-principles code. RECIPE provides a complete dimensional history and the time-dependent spectral power at 56 wavelengths from 0.2 to 12.5 μm with approximately 0.02 μm resolution in the 0.2 to 1.0 μm range. It has been extended to include surface bursts. Although based on theoretical modeling, the second peak flux of the airburst source module has been validated dimensionally against extensive test data. The surface-burst source module also agrees well with the limited amount of available test data. The air transmission module takes into account the attenuation processes due to molecules and aerosol scattering, and absorption due to water vapor, carbon dioxide, and ozone. However, as noted above in discussing the first thermal peak, RECIPE does not account for nonequilibrium chemical species associated with the fireball.

6.2.1 Fireball Expansion. The relationship between radius of the fireball and yield for both low-altitude and surface bursts is:

$$R \text{ (at thermal minimum)} \approx 27 \ W^{0.4} , \tag{6.2}$$

where R is the fireball radius in meters and W is the yield in kilotons. The radius at breakaway of the weakly luminous shock front from the fireball is different for air and surface bursts:

Airbursts: R (at breakaway) $\approx 34 \ W^{0.4}$, $\quad$ Surface: R (at breakaway) $\approx 44 \ W^{0.4}$. $\quad$ (6.3 & 6.4)

The RADFLO physics code provides the following altitude-dependent fireball and shock radii data for air bursts at the time of the second thermal maximum. It is accurate up to about 50 km altitude:

$$R_{FB} \ (t_{2max})(m) = 51.8 \ W^{0.372} \ \rho^{-0.14} , \qquad R_{SHOCK} \ (t_{2max})(m) = 83.5 \ W^{0.383} \ \rho^{-0.14} , \quad (6.5 \ \& \ 6.6)$$

where $\rho = \rho_A/1.225$, and ρ_A is the ambient density in grams per liter at the burst altitude.

RECIPE data on fireball radius versus time for various altitudes are shown in Figures 6.2 to 6.6 for yields from 1 KT to 10 MT. The 0 km altitude curves correspond to a contact surface burst. These curves are estimated to be reliable to about ±15 percent in both time and distance.
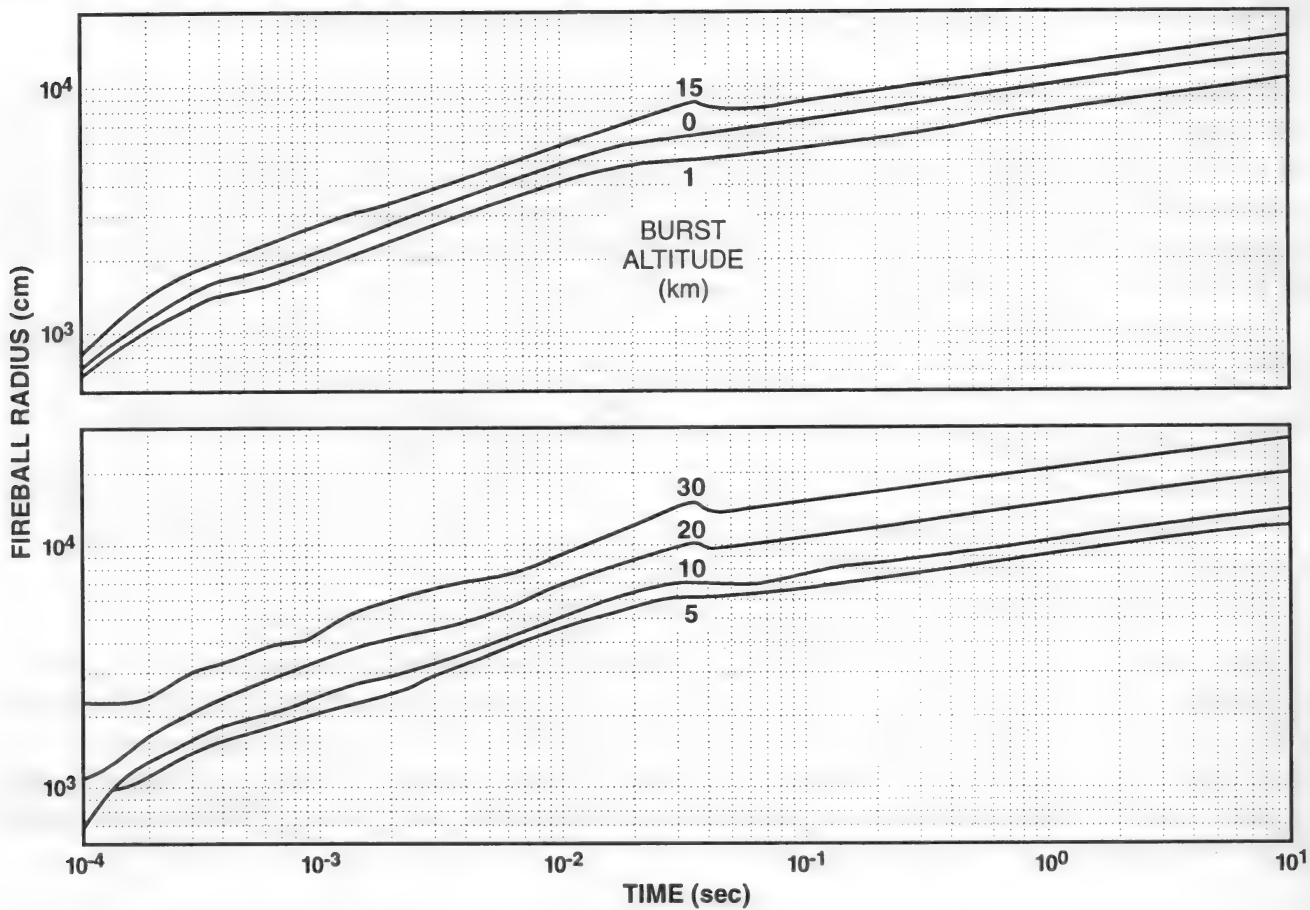
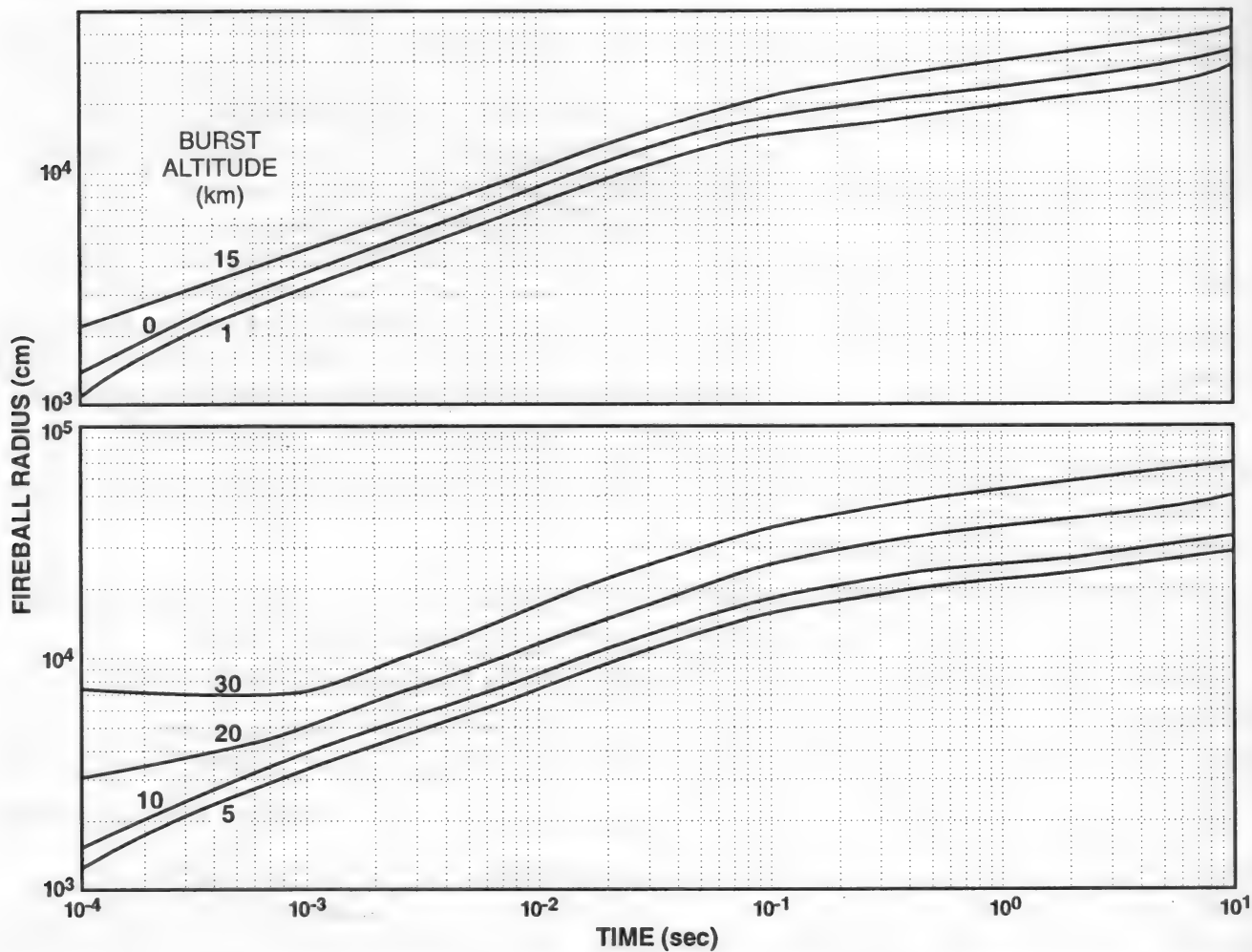**Figure 6.2.** Fireball Radius Versus Time Curves for a 1-KT Burst at Various Altitudes.

Figure 6.3. Fireball Radius Versus Time Curves for a 10-KT Burst at Various Altitudes.
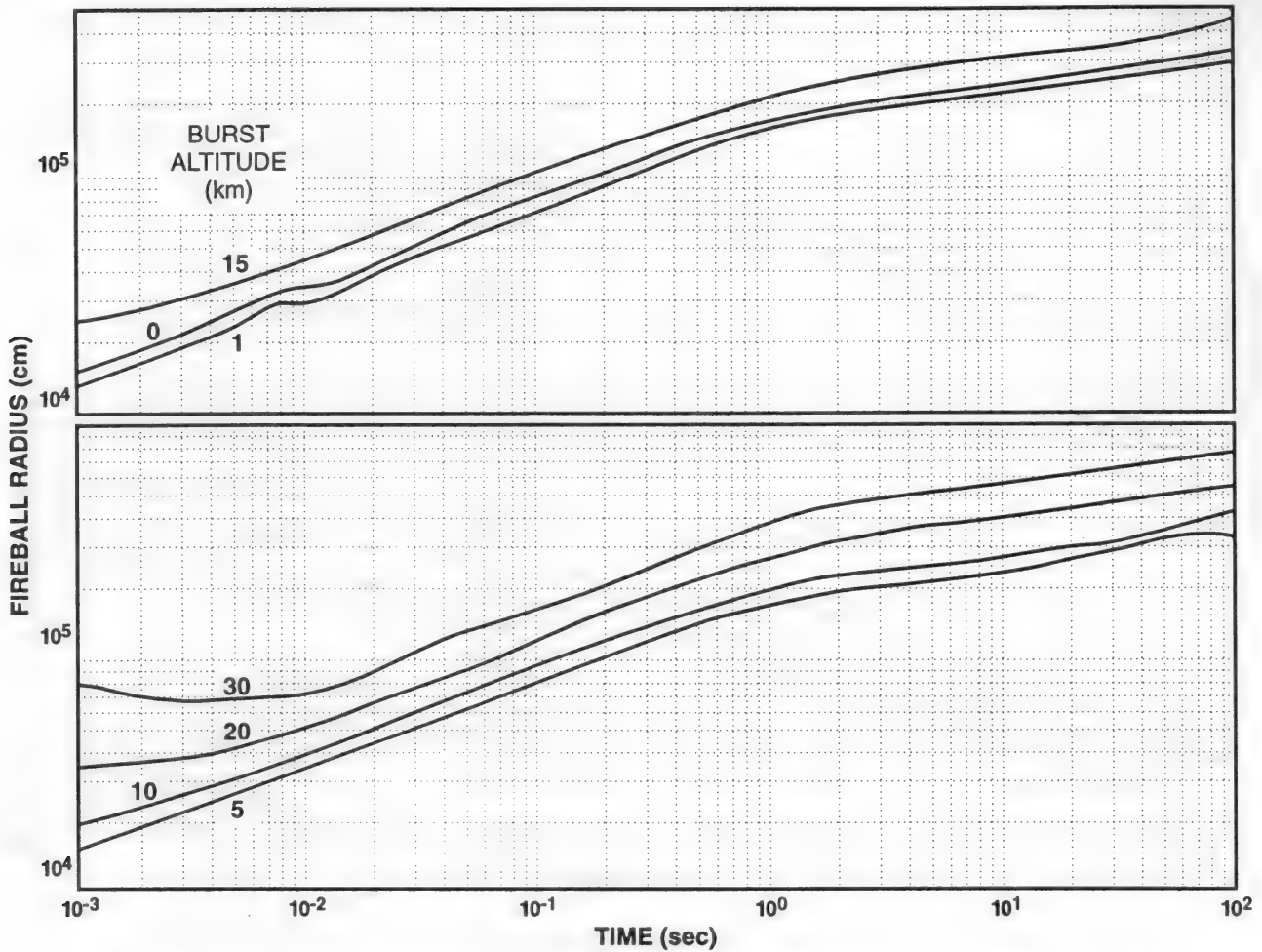
Figure 6.6. Fireball Radius Versus Time Curves for a 10-MT Burst at Various Altitudes.

6.2.2 Thermal Yield Fraction. The thermal yield fraction, or thermal partition, is the fraction of the total energy which appears as thermal output, E_{tot}/W. Figure 6.7 shows it as a function of yield for several altitudes from 1 to 30 km. In practice the thermal energy emitted over extended times is of little military significance, and it is frequent practice to terminate the integration at some multiple of the thermal maximum time, e.g., $10 \, t_{2max}$. At very low heights of burst ($< 4 \, W^{1/3}$ meters) the inclusion of surface material into the fireball radically changes the thermal fraction. Surface burst values are shown in Table 6.1.

The RADFLO data are based on the following expressions for total radiant energy, E_∞(KT).
Surface Burst: $0.149 W^{1.024}$;   Free Air (< 4.3 km): $0.350 \, W$.   (6.7)
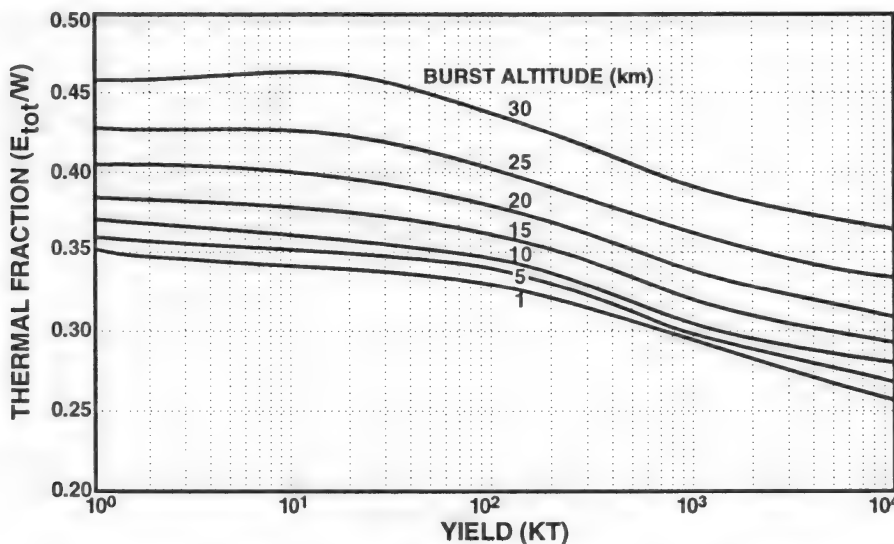
Figure 6.7. Thermal Yield Fraction as a Function of Burst Altitude and Yield (Altitude Contours).

Table 6.1. Thermal Fraction Values for Near-Surface Bursts.

	RECIPE			RADFLO	
Yield (KT)	Surface Burst Thermal Fraction	Nonsurface Burst Thermal Fraction	Transition Height (meters)	Surface Burst Thermal Fraction	Nonsurface Burst Thermal Fraction
1	0.045	0.35	4	.149	.350
10	0.066	0.34	8.6	.157	.350
100	0.13	0.33	18.5	.166	.350
1,000	0.16	0.31	40	.176	.350
10,000	0.17	0.26	86	.186	.350

6.2.3 Thermal Power Versus Time.

Table 6.2 is a summary of the empirical thermal radiation scaling laws.

Table 6.2. Summary of the Empirical Thermal Radiation Scaling Laws.

Parameter	Surface Bursts	Free Air < 4.3 km	Free Air > 4.3 km
t_{min} (ms)	4.25 $W^{0.44}$	3.13 $W^{0.44}$	4.3 $W^{0.45}$ $\rho^{0.23}$
t_{2max} (ms)	41.93 $W^{0.464}$	41.7 $W^{0.44}$	40.0 $W^{0.45}$ $\rho^{0.35}$
P_{2max} (KT/s)	1.35 $W^{0.56}$	3.18 $W^{0.56}$	3.1 $W^{0.55}$ $\rho^{-0.54}$
E_{10max} (KT)	0.118 $W^{1.024}$	0.277 W	0.276 W $\rho^{-0.034}$

t_{min} = time to the first minimum for the fireball as a blackbody

t_{2max} = time to the second maximum

P_{2max} = power at the time of the second maximum.

E_{10max} = thermal energy radiated prior to 10 times t_{2max}

W = yield (KT) (Note: 1 KT = 10^{12} calories)

An analytical approximation to the time-dependent thermal power, P(t), for the second peak of low airburst is:

$$P(t) / P_{2max} = 2t^2 / (1 + t^4),\tag{6.8}$$

where t is the normalized time (t/t_{2max}). Figure 6.8 shows this curve of normalized power and percen of total energy emitted versus normalized time. Figures 6.9 to 6.13 give the results of RECIPE calcu lations of the source power versus time for a set of altitudes, for each decile of yield.
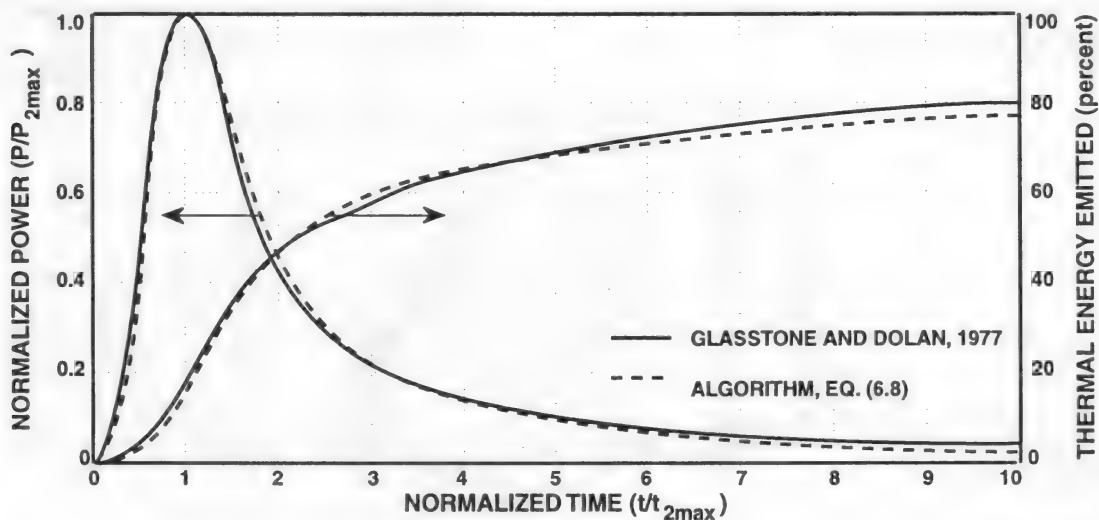

Figure 6.8. Normalized Power and Percent of Total Thermal Energy as a Function of Normalized Time.
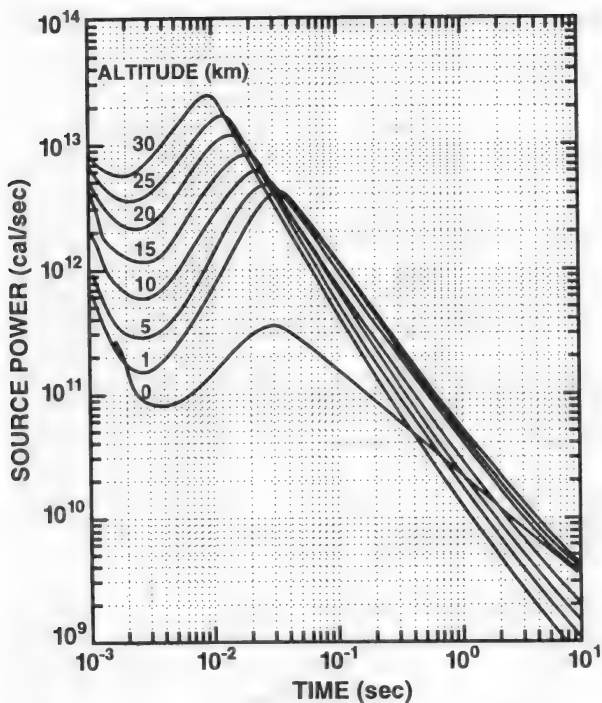
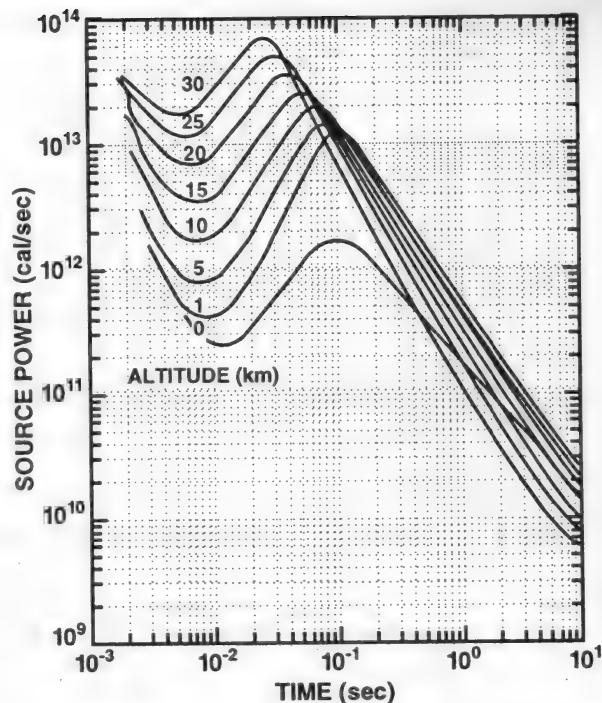**Figure 6.9.** Effects of Altitude on Thermal Power for a 1-KT Burst.

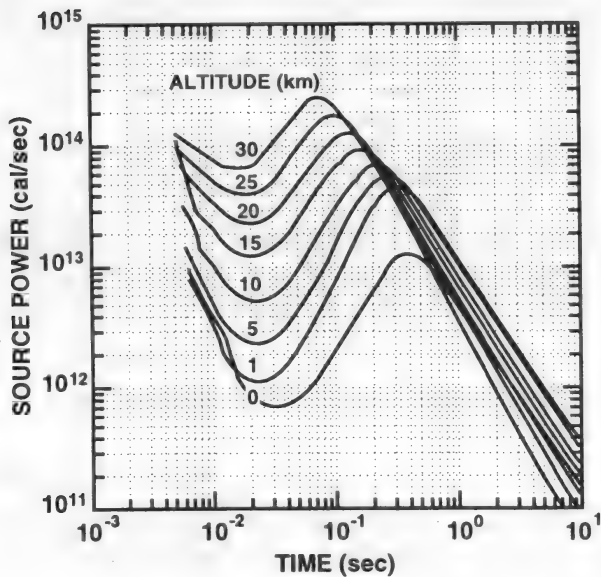**Figure 6.10.** Effects of Altitude on Thermal Power for a 10-KT Burst.

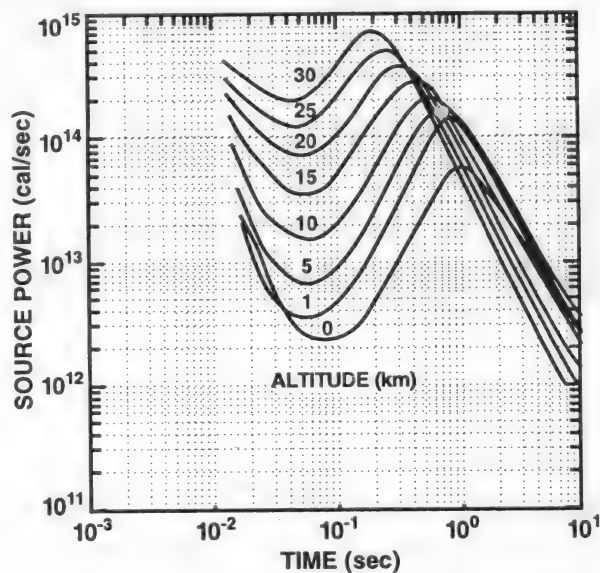**Figure 6.11.** Effects of Altitude on Thermal Power for a 100-KT Burst.

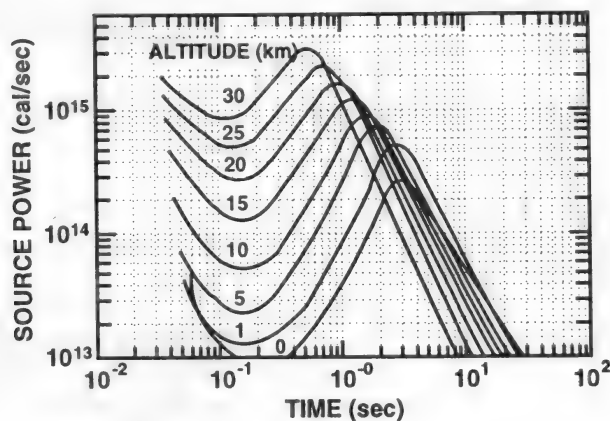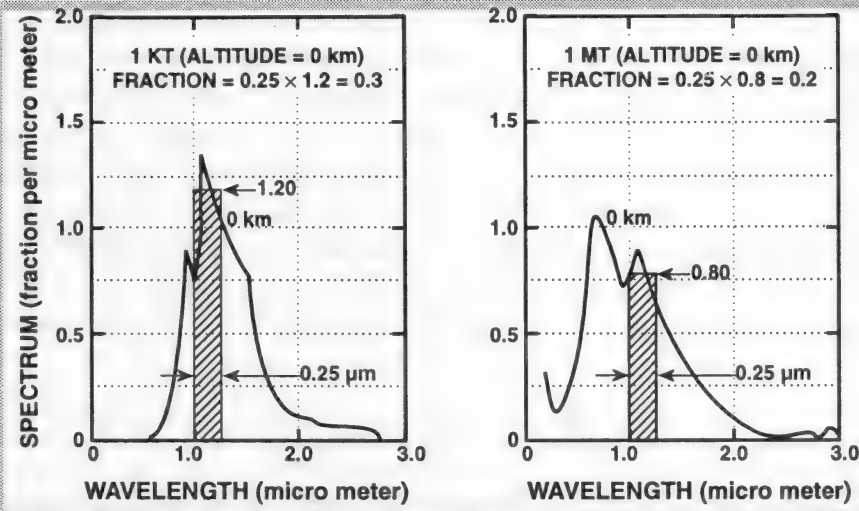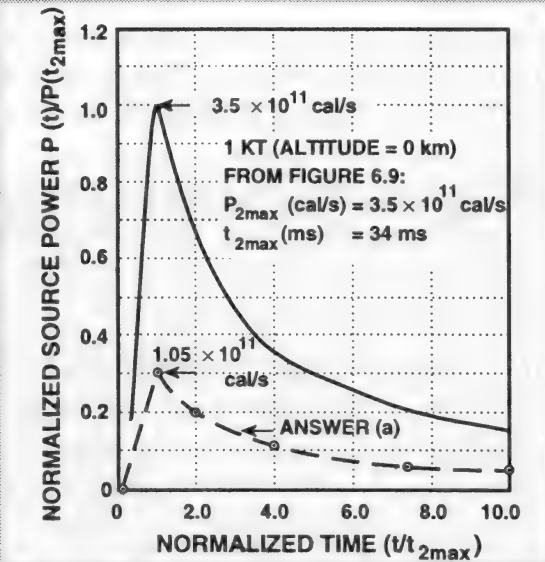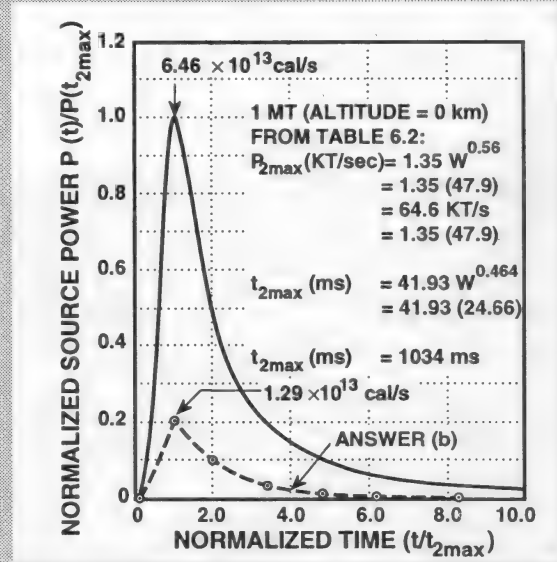**Figure 6.12.** Effects of Altitude on Thermal Power for a 1-MT Burst.

Figure 6.13. Effects of Altitude on Thermal Power for a 10-MT Burst.

(a) Spectral Distributions

(b) Power vs. Time for a 1-KT Surface Burst
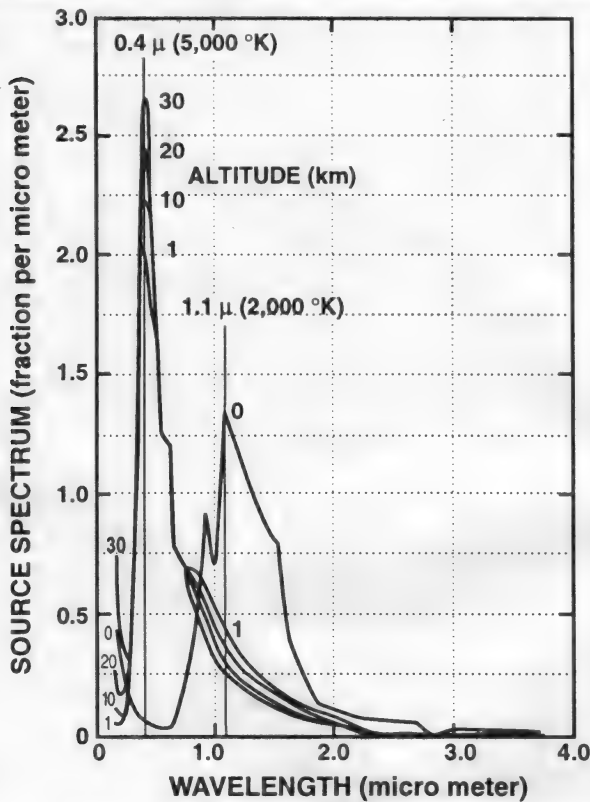

(c) Power vs. Time for a 1-MT Surface Burst

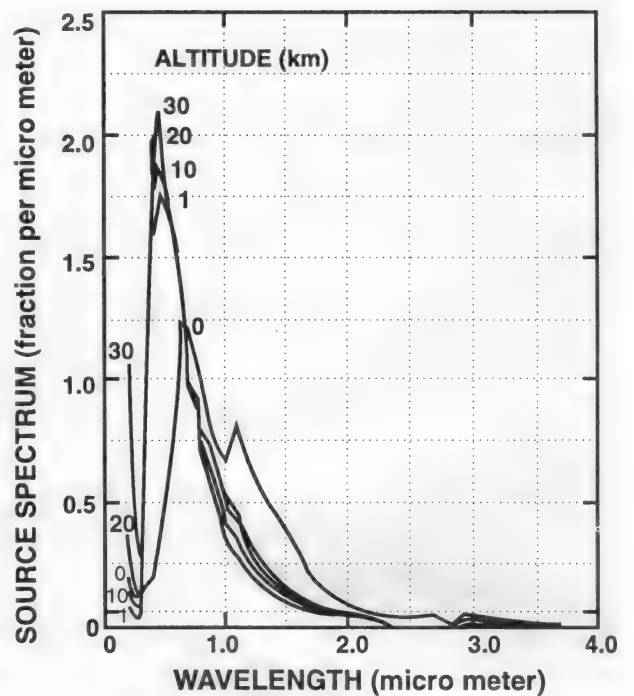**Figure 6.19.** Effects of Altitude on Spectral Distribution for a 1-KT Burst.

Figure 6.20. Effect of Altitude on Spectral Distribution for a 100-KT Burst.
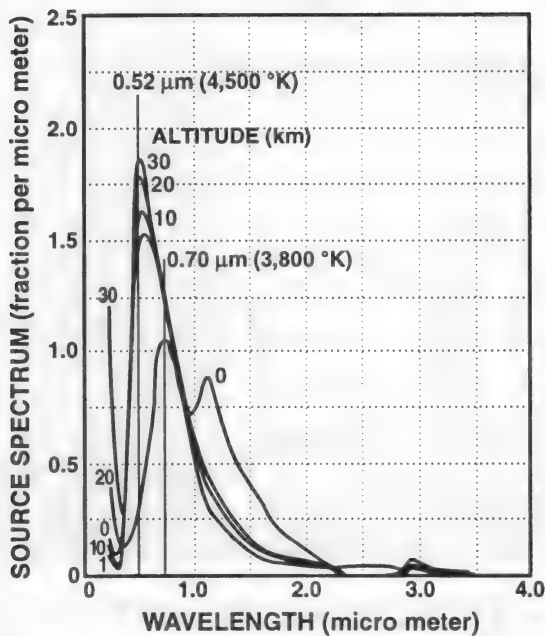
Figure 6.21. Effect of Altitude on Spectral Distribution for a 1-MT Burst.

6.2.6 Thermal Exposure. This section includes several families of curves of radiant exposure (cal/cm^2) versus range for various parameters. Factors which influence the data are the thermal fraction, HOB, visual range, yield, and target altitude. All assume a target with its normal oriented towards the source, and no albedo from the earth's surface or clouds. Limited data sets are provided based on RECIPE. More complete sets of figures are provided in *EM-1*, Chapter 6. Figures 6.22 through 6.27 show exposure as a function of target altitude versus ground range for surface and 1-km burst altitudes for several combinations of yield and visibility. Figures 6.28 through 6.37 provide thermal exposure curves for a target on the ground, as contours of HOB versus ground range, for various yields and visibilities. Also shown on these figures for comparison are airblast peak overpressure on the ground under the same burst conditions.

Sample Problem 6.4 Determining Thermal Exposure on Targets. For a target at 8-km altitude and a 300-KT burst at (a) the surface and (b) 1-km altitude, find the slant ranges for both burst altitudes corresponding to exposure of 20 cal/cm^2 on the target.

(a) Using the total thermal fraction from Table 6.1 to obtain the ratio 300 KT to 1,000 KT outputs:

$$(fW)_{300} / (fW)_{1,000} = (0.14 \times 300) / (0.16 \times 1,000) = 0.26$$

Thus, 20 cal/cm^2 for 300 KT is at the same contour level as $20/0.26 = 76.9$ cal/cm^2 on Figure 6.26. 80 cal/cm^2 (1,000 KT) only reaches 5.2 km; thus 20 cal/cm^2 from 300 KT will not reach 8 km. Note that the exposure at 8 km altitude for 1 MT is approximately 40 cal/cm^2, or for 300 KT, about 10 cal/cm^2.

(b) Thermal ratio (1 km burst) (Figure 6.7): $(fW)_{300} / (fW)_{1,000} = (0.315 \times 300) / (0.29 \times 1,000) = 0.33$
20 cal/cm^2 for 300 KT is the same contour as $20/0.33 = 60.6$ cal/cm^2 at 1,000 KT (Figure 2.6).
Using R^{-2} interpolation over the short distance in the clear air from the 50 km contour (7.7 km above the burst; Figure 6.26), the 300 KT fluence at 8 km is only: $(50) (7.7/8)^2 (0.33) = 15.3$ cal/cm^2

Sample Problem 6.5 Determining Thermal Exposure/Airblast on Targets. (a) For a 5-KT burst at 0.4 km altitude, find the thermal exposure on the ground where the peak overpressure is 10 psi, and the times of arrival of the thermal pulse and the peak overpressure.

Scaled height of burst:	$SHOB = 0.4/(5)^{1/3} = 0.4/1.71 = 0.23$ km
Scaled ground range for 10 psi contour and 0.23 km SHOB (Figure 6.28):	$SGR = 0.4$ km
Ground range:	$GR = 0.4(5)^{1/3} = 0.68$ km
Thermal exposure for 1 KT at GR = 0.68 km and HOB = 0.4 km (Figure 6.28):	4.5 cal/cm^2
Relative thermal outputs (Figure 6.7):	$(fW)_5/(fW)_1 = (0.34 \times 5)/(0.35 \times 1) = 4.9$
Thermal exposure for the 5 KT case:	$Q = (4.5)(4.9) = 22.5$ cal/cm^2
Arrival time of second thermal peak (Table 6.2):	$t_{2max} = 41.7(5)^{0.44} = 84.7$ ms
Arrival time of airblast, 1 KT (Figure 2.44, interpolating between contours):	0.85 s/$KT^{1/3}$
Airblast arrival, 5 KT (Eq. 2.15):	$0.85(5)^{1/3} = 1.45$ s

(b) For a 600-KT burst at 5 km altitude, find the peak overpressure where the thermal exposure on the ground is 50 cal/cm^2.

Thermal fraction ratio (Figure 6.7):	$(fW)_{600}/(fW)_{1,000} = (0.31 \times 600)/(0.31 \times 1,000) = 0.6$
The 1-MT contour equivalent to 50 cal/cm^2 and 600 KT is thus:	$50/0.6 = 83.3$ cal/cm^2
Using the 80 cal/cm^2 contour intersection with HOB = 5 km (Figure 6.34):	$GR = 1.75$ km
Equivalent for 1 MT: $R = 1.75(1,000/600)^{1/3} = 2.065$ km; $HOB = 5(1,000/600)^{1/3} = 5.9$ km	
Overpressure at this range for this HOB (Figure 6.34):	about 5 psi

6.3 Atmospheric Transmission Effects. As introduced in Equation 6.1, transmission effects are given by the product Tg, where T is the transmittance factor for a generalized geometry with idealized albedo surfaces and model atmospheres depending on the visibility. The geometry factor g includes fireball asymmetry and target orientation effects. Values of T and g have been computed for a wide variety of situations and are presented in graphical form for predictive purposes. Such predictions are intended only to bracket a particular case for which actual transmission factors will vary with time and space, and may be very difficult to specify quantitatively. In addition, the normal variables of humidity, dust, haze, fog, smog, and albedo factors will be even less predictable in rapidly changing wartime environments.

The codes used to produce these data compute both the direct and scattered components as a function of wavelength over the range between 0.3 and 4.0 μm. Scattering includes both Rayleigh (molecular) and Mie (aerosol), and absorption is calculated for water vapor, carbon dioxide, and ozone. The cross sections for all of these processes are wavelength dependent.

Thus, it is customary to define discrete wavelength bands and perform the transport calculations with the scattering and absorption parameters defined over the separate bands. The "buildup factor" is the ratio of the total exposure to directly transmitted exposure, and thus is a measure of the importance of the scattered or diffuse component of the radiation. Figure 6.38 illustrates this factor as a function of optical depth (integral of the product of the scattering cross section and number density of the scattering medium along the path from source to detector) for Pacific Test Site conditions and the albedo of seawater, and shows that the diffuse component may be much larger than the direct component at long ranges. The resulting angular distribution for one wavelength (0.55 μm) is shown in Figure 6.39.

6.3.1 Effects of Meteorological Conditions. This section considers the effects of aerosols and molecular absorption. Albedo effects will be discussed in Section 6.3.2.

6.3.1.1 Visibility. Daylight visibility is the distance at which a large dark object is just recognizable against the sky background. Nighttime visibility is defined as the longest distance at which an unfocused light of moderate intensity can be seen. Table 6.3 gives the international visibility code, relating a qualitative description of the atmosphere to observed visibilities. It is usually assumed that the transmittance is 5.5 percent along the distance corresponding to the visibility.

The "meteorological range" (MR) is the horizontal distance for which the transmittance of the atmosphere for a direct beam of light is 2 percent. The meteorological range is related to the atmospheric extinction cross section by:
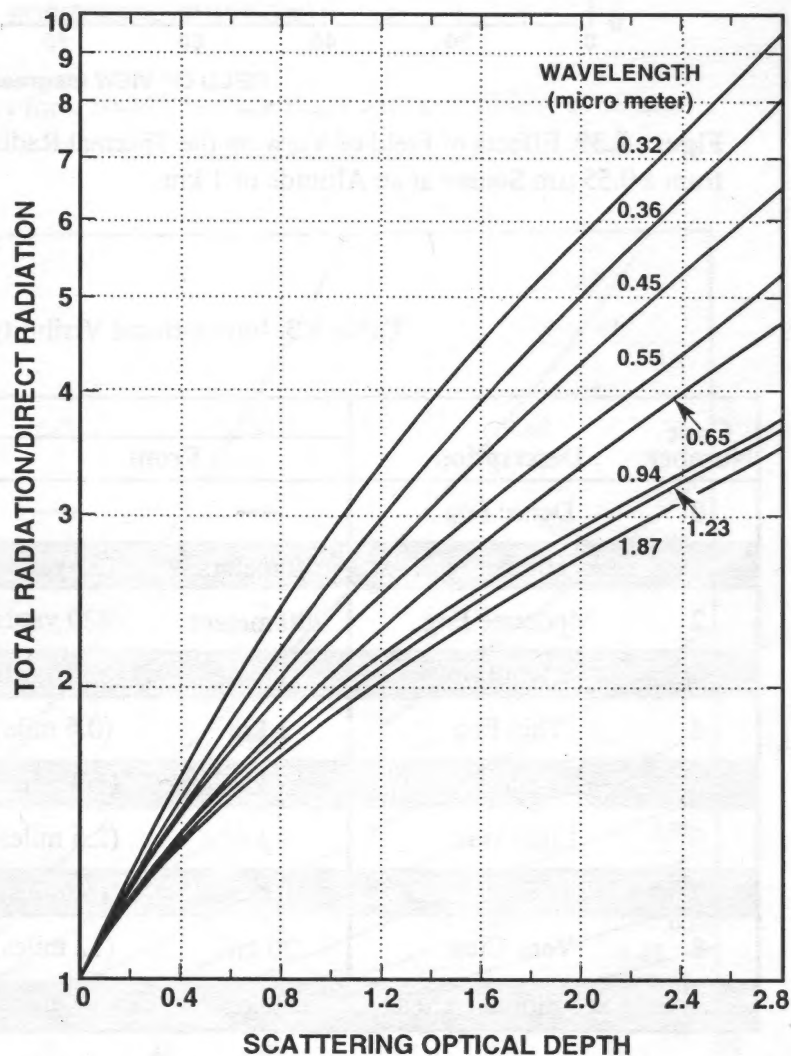
$$\sigma_T = 3.91/\,MR \qquad (6.8)$$

Figure 6.38. Comparison of Buildup Factors for Various Radiation Wavelengths Simulating Pacific Atmosphere with Both Source and Sampling at 1-km Altitude.

The relationship between the visibility and the meteorological range is:

$$V = 0.74 \; MR .$$ (6.9)

In this section, all transmission predictions will be related to the visibility, and not to the meteorolog-
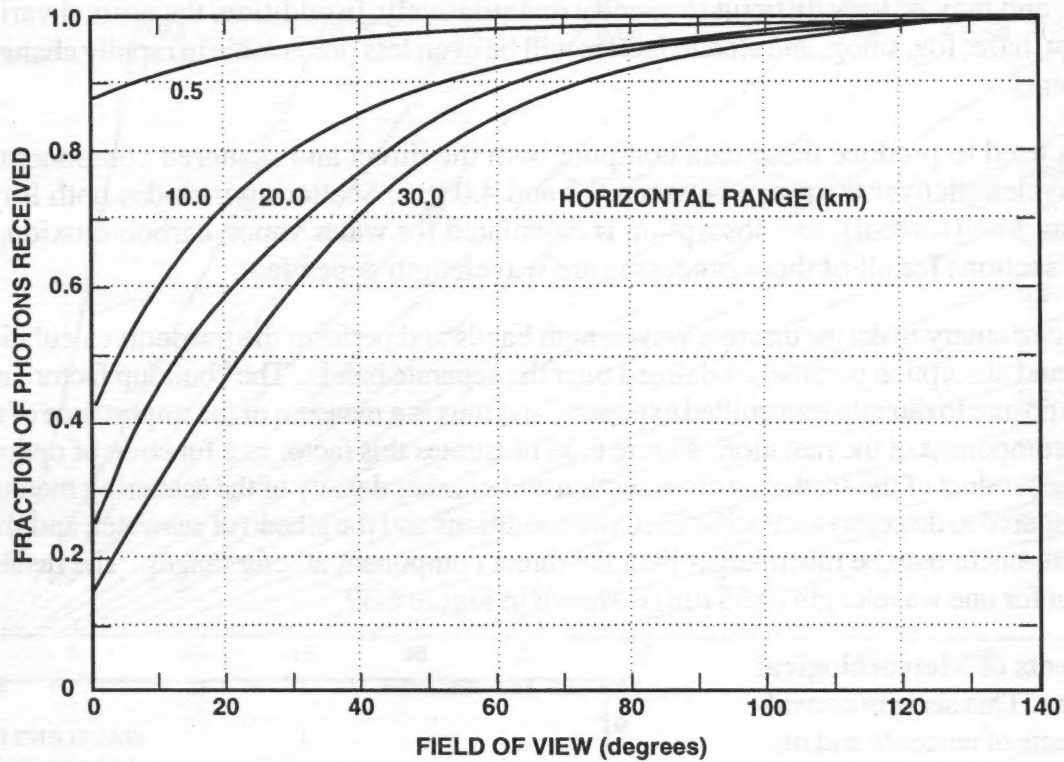ical range.

Figure 6.39. Effects of Field of View on the Thermal Radiation for a Target on the Ground
from a 0.55 μm Source at an Altitude of 1 km.

Table 6.3. International Visibility Code.

| Code Number	Description	Visibility			
		From		To	
0	Dense Fog	—	—	50 meters	(55 yards)
1	Thick Fog	50 meters	(55 yards)	200 meters	(220 yards)
2	Moderate Fog	200 meters	(220 yards)	500 meters	(550 yards)
3	Light Fog	500 meters	(550 yards)	1 km	(0.6 mile)
4	Thin Fog	1 km	(0.6 mile)	2 km	(1.2 miles)
5	Haze	2 km	(1.2 miles)	4 km	(2.5 miles)
6	Light Haze	4 km	(2.5 miles)	10 km	(6 miles)
7	Clear	10 km	(6 miles)	20 km	(12 miles)
8	Very Clear	20 km	(12 miles)	50 km	(30 miles)
9	Exceptionally Clear	50 km	(30 miles)	—	—
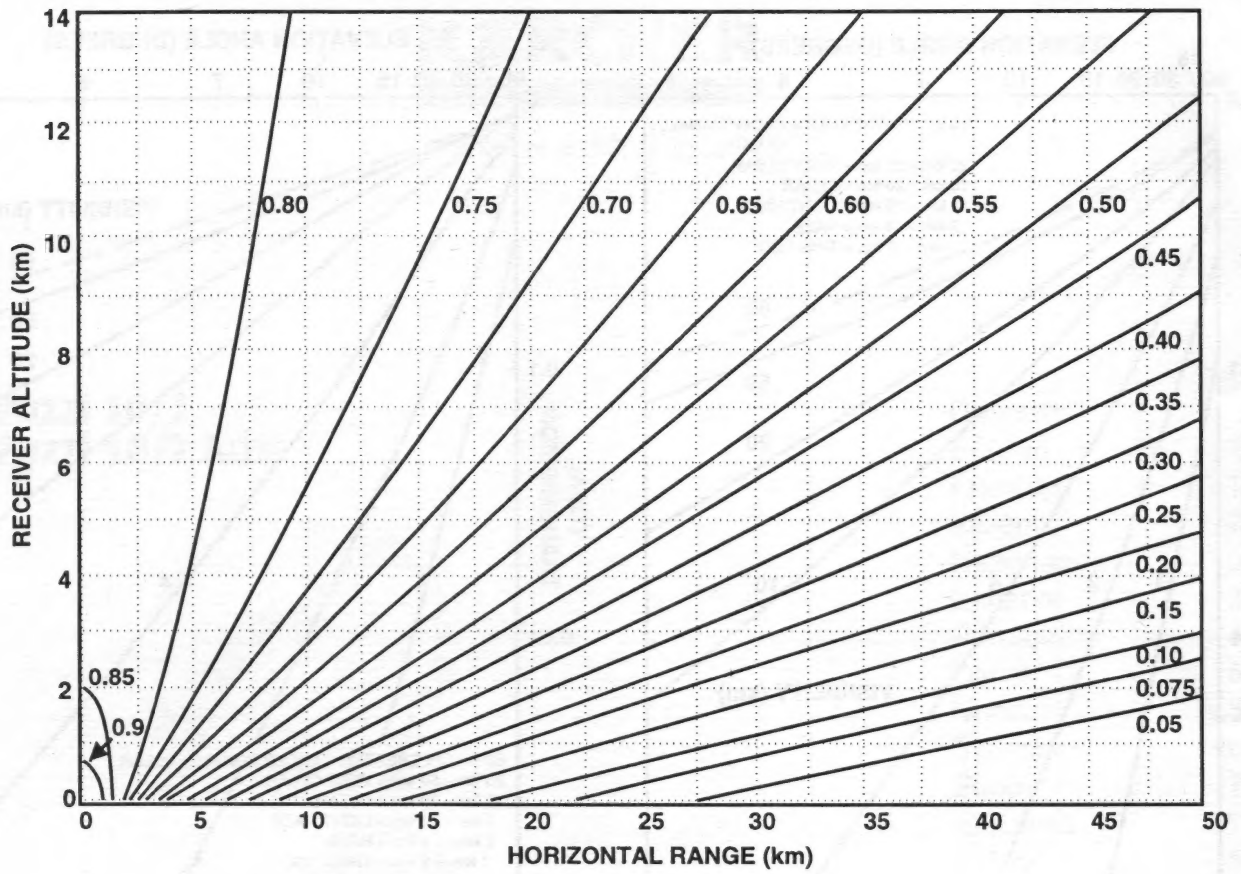
Figure 6.46. Transmission Contours for a 10-MT Surface Burst with a Visibility of 10 km.
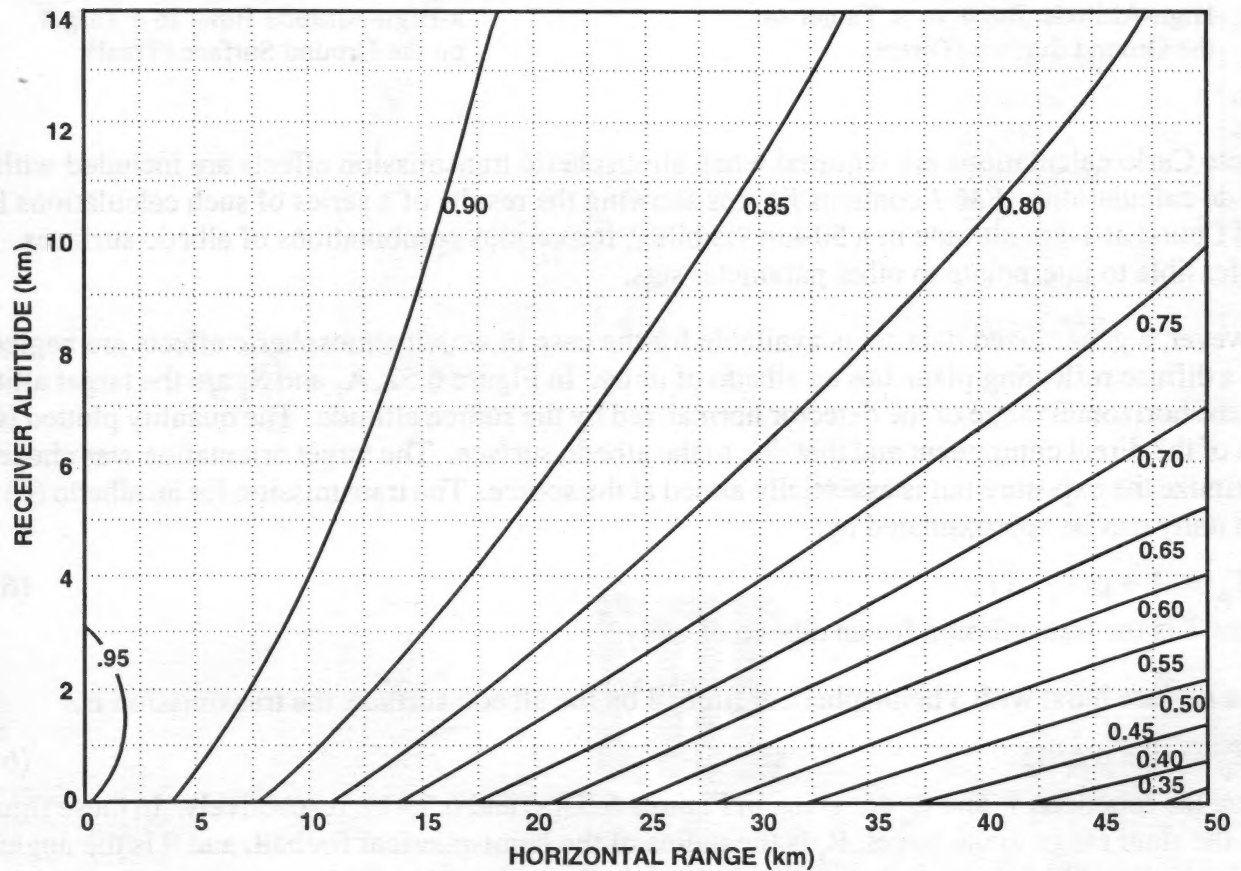

Figure 6.47. Transmission Contours for a 1-MT Burst at an Altitude of 1 km with a Visibility of 50 km.
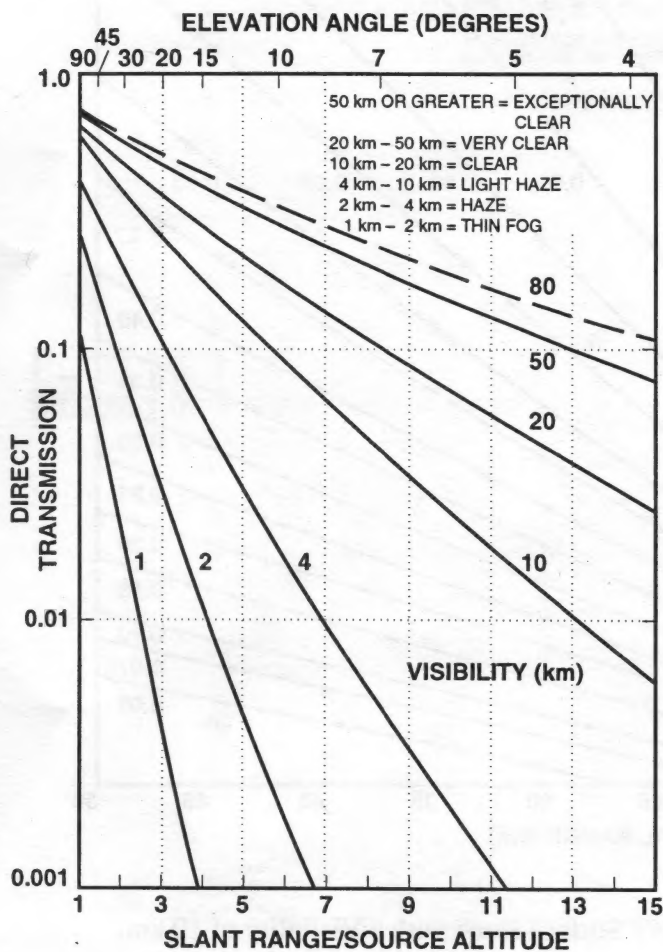
ELEVATION ANGLE (DEGREES)

Figure 6.48(a). Transmission from a High-Altitude Burst to a Target on the Ground Surface (Direct).
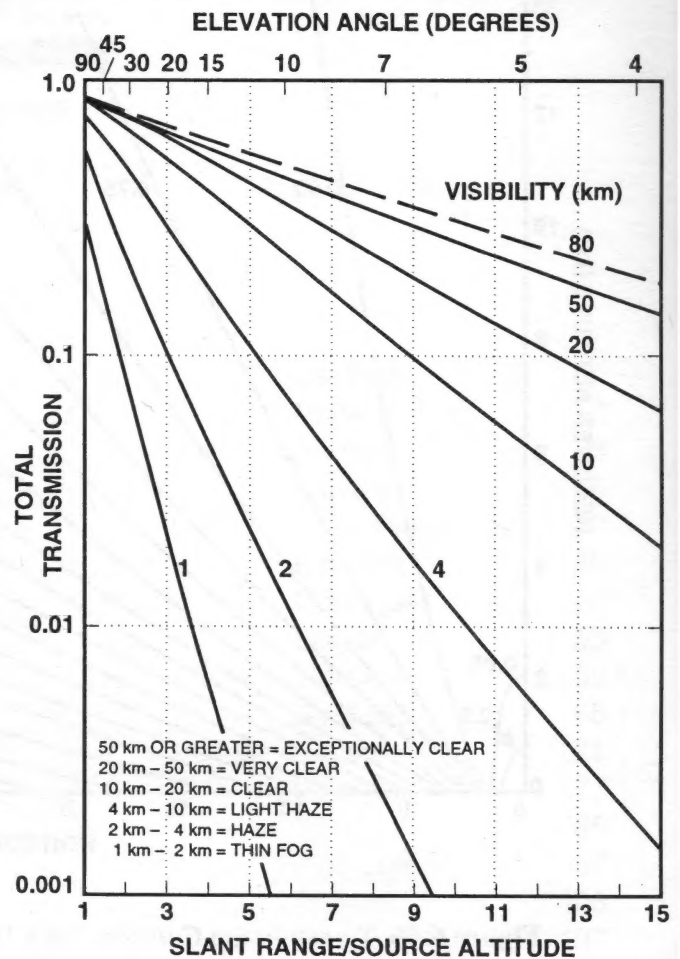
Figure 6.48(b). Transmission from a High-Altitude Burst to a Target on the Ground Surface (Total).

Monte Carlo calculations are required when atmospheric transmission effects are included with the albedo calculations. *EM-1* contains figures showing the results of a series of such calculations for a 1-MT burst at 1-km altitude in a 50-km visibility, for various combinations of albedo surfaces. It is not feasible to interpolate to other parameter sets.

However, a generalized data set is available for the case in which atmospheric effects are neglected and a diffuse reflecting plane has an albedo of unity. In Figure 6.52, A_1 and S_1 are the target altitude and the horizontal range of the detector normalized by the source altitude. The quantity plotted is the sum of the direct component and that due to the albedo surface. The target orientation was chosen to maximize the exposure but is essentially aimed at the source. The transmission for an albedo (ρ) less than unity can be approximated by:

$$T_\rho = 1 + \rho(T_1 - 1),$$ (6.12)

where T is the transmission for an albedo of unity.

For a surface burst with a hemispherical fireball on the albedo surface, the transmission is,

$$T_\rho = 1 + \rho\gamma_n/\eta_n.$$ (6.13)

where the functions γ_n and η_n are given in Figures 6.53(a) and 6.53(b), respectively. In these figures, R is the slant range to the target, R_s is the radius of the hemispherical fireball, and θ is the angle between a vertical line through the burst point and the line of sight to the target.